Check for updates

Tuning oxidative propane dehydrogenation while co-converting CO_2 over vanadium containing CHA zeolites

Jose A. Mendoza Mesa, [iD] †[a] Meera A. Shah, [iD] †[a] Marco G. Rigamonti, [iD] †[a] Pierre Eloy, [iD][b] Damien P. Debecker, [iD][b] Iqtidar Ali Khan, [iD][a] Ibrahim Khalil [iD][a] and Michiel Dusselier [iD] *[a]

Propane dehydrogenation (PDH) is an essential industrial process for on-purpose propene production, but current technologies face equilibrium limitations and severe coking. Using CO_2 as a soft oxidant can reduce coking, enhance propene yield, and convert the greenhouse gas into CO, a platform chemical. An exclusive CO_2-based oxidative catalyst has not been reported because when feeding soft oxidants, concomitant routes - oxidative and non-oxidative - are present. We prepared vanadium supported on CHA zeolites (and alumina as a benchmark) by modulating the vanadium loading but also the zeolite particle size and their aluminum content (Si/Al ratio) and the samples were characterized by X-ray Diffraction (XRD), temperature-programmed reduction with hydrogen (H_2-TPR) and X-ray photoelectron spectroscopy (XPS), among other techniques. The role of the acidity in side-reactions is that it encourages coke formation rather than propane cracking. Catalyst with small crystals showing better metal dispersion, and likely from that high activity and stability. Small zeolite particle size and low acidity seem essential attributes for better V/small pore zeolite catalyst design. Interestingly, the V/CHAs activity are favorably impacted by working at higher pressure compared to the impact on the benchmark γ-Al_2O_3 support. The optimal metal loading range was investigated between 0.6 mmol $g^{-1}_{support}$ and 2.6 mmol $g^{-1}_{support}$, with an eye on both propylene production and co-production of CO as well as deactivation and its relation to coke formation. The catalytic performance evaluation covers a set of experiments with different conditions and next to classic conversion, selectivity and yield numbers, we display molar rates in the form of a unique box and whisker analysis. This provides a comprehensive view of the catalytic performance and allows comparing multiple time-on-stream (TOS) profiles of multiple products and reagents all in one plot. The best material, V/CHA70, combines a small particle size and the highest Si/Al ratio tested here. With a vanadium load of 1.3 mmol $g^{-1}_{support}$ this material achieves a conversion of 33.9% for propane simultaneous co-conversion of CO_2 of 21.3% with a propylene rate of 8.4 mol h^{-1} kg^{-1} at initial TOS. Moreover, the material demonstrates excellent cyclability and the highest stability within the set of samples, showing a decrease of only 0.6% per regeneration cycle, ensuring good activity even after 10 regenerations and 25 hours of reaction in near-industrial conditions.

1. Introduction

Due to its use in the polymer industry, the increasing demand for propylene brought substantial attention to the study of propane dehydrogenation (PDH).[1,2] The cracking of naphtha and the fluid catalytic cracking of heavier hydrocarbon fractions dominate current propylene production and because of these propylene has a significant greenhouse gas (GHG) footprint, *i.e.* on average worldwide 2.8 tons of CO_2-equivalents per ton. On top, the reliance on side-streams and cracking cannot meet upticks in demand and thus, on-purpose propylene production technologies are becoming essential to fulfil the supply/demand gap.[1,3,4] In particular, propane dehydrogenation is the leading on-purpose technology for propylene production, accounting for about 22% of the supply–demand gap in 2018, with its contribution expected to rise to 32% by 2027.[5] Commercially, PDH is mainly carried out by Cr or Pt-based catalysts. However, due to the endothermic nature of the reaction, the required high

[a] *Center for Sustainable Catalysis and Engineering (CSCE), KU Leuven, Celestijnenlaan 200F, 3001 Heverlee, Belgium.*
E-mail: michiel.dusselier@kuleuven.be
[b] *Université catholique de Louvain (UCLouvain), Institute of Condensed Matter and Nanosciences (IMCN), Place Louis Pasteur, 1, box L4.01.09, 1348 Louvain-la-Neuve, Belgium*
† Equal contribution.

This journal is © The Royal Society of Chemistry 2025

Catal. Sci. Technol., 2025, **15**, 5295–5317 | **5295**

temperatures result in thermal cracking and coking, leading to catalyst deactivation. Therefore, new catalysts with increased activity, stability, and selectivity are greatly desired.[1,6]

Oxidative propane dehydrogenation (OPDH) has been suggested as an alternative to traditional PDH to decrease catalyst deactivation (less coke formation) and improve thermodynamic limitations.[7] However, the challenge imposed by fully oxidizing propane and propylene to carbon oxides is present when using O_2. Using carbon dioxide (CO_2), a weaker oxidant, can counteract this issue while offering sustainability benefits.[8,9] We recently published a preliminary life cycle assessment demonstrating that revamping current PDH processes to consume industrial CO_2 flue gas can, on paper, reduce greenhouse gas emissions (GHG) by 8 to 13 $MtCO_{2\text{-eq}}$ y^{-1} (−0.3 to −0.5 $kg_{CO_2 \text{ - eq}}$ per $kg_{propylene}$). CO_2-OPDH catalysis can either proceed *via* an indirect route, where reverse water gas shifts (rWGS) reaction occurs in series to normal PDH (Indirect route eqn 2.1 + 2.2, Table 1), or *via* a direct route (eqn (3)).

The benefit of OPDH *via* a catalyst that proceeds *via* a direct redox pathway seems to outweigh the added complexity – and environmental costs – to separate and recycle CO_2, CO, H_2, and H_2O, lowering emissions between 15% and 50% of kg of CO_{2eq} per kilogram of propylene produced *versus* non-oxidative PDH (1.5 kg_{CO_2} $kg_{propylene}^{-1}$), mainly from consuming CO_2. Even the potential for negative net emissions is quite significant, provided that the co-produced CO replaces (in part) the established but quite polluting route of steam methane reforming.[10] Co-producing CO at the expense of H_2, which forms H_2O, could be beneficial since CO is a chemical with a higher environmental impact compared to H_2 (3-fold GHG and 5-fold fossil fuel depletion impact). Separation of residual H_2 from CO is also not necessary, since many applications of CO require H_2 (syngas).

In the presence of CO_2 as an oxidant, it is widely acknowledged that propylene is produced *via* all three routes shown in Table 1. In summary, route 1 is PDH, route 2 is two consecutive reactions of PDH + RWGS, and the third one is CO_2-OPDH. However, the literature categorization on route CO_2-OPDH does not often attempt to distinguish between a coupled reaction (one catalytic cycle, route 3) or a consecutive reaction (two catalytic cycles, route 2). Furthermore, a fourth route has barely been reported under non-oxidative conditions: propane dehydrogenation using[11] stoichiometric

lattice oxygen from the metal oxide. Several kinetic models have been proposed based on studies of such oxygen-free atmosphere under the Chemical Reactor Engineering Center riser simulator.[12–14] Sometimes, papers on OPDH with CO_2 report the CO/C_3H_6 and H_2/C_3H_6 ratios with the intention to broadly classify oxidative and non-oxidative catalytic performance and materials. However, the complexity of the reaction network and the occurrence of side reactions are the main limitations of this approach.[15]

Vanadium, a versatile metal with relatively low toxicity, *e.g.* as compared to Cr, possesses tunable properties,[16,17] such as several oxidation states, polymerization degree, and multiple deposition strategies that render it suitable for selective oxidation reactions such as O_2- or CO_2-OPDH.[7,18–22] Our comprehensive screening of over 20 elements on γ-alumina, with a specific focus on CO_2 and propane conversion, confirmed this property.[10] The productivity - expressed as molar rates- of both CO and propylene (10 and 6 mol h^{-1} kg_{cat}^{-1}) is only surpassed by gallium and chromium-based catalysts, which do not facilitate direct redox mechanisms and an efficient co-conversion of CO_2.[10] The most commonly hypothesised mechanism for vanadium (and other redox materials) is the Mars–Van Krevelen (MvK) process. In this process, CO_2 can partially reoxidise the reduced vanadium metal oxides formed during propane activation, demonstrating the critical role of vanadium in this catalytic mechanism.[13,23–26]

Understanding vanadium activity in catalysis presents significant challenges due to the lack of consensus regarding the speciation and polymerisation degree of chemical species.[27–30] In a study of vanadium species deposited on alumina following the PDH reaction, Xiong *et al.*[28] describe the concurrent reactions. The prevalence of V=O species was associated with a dominance of the oxidative pathway, and once this disappeared through the redox pathway, the PDH regime became predominant. Even with the introduction of oxidative agents, only a fraction of propylene was typically produced *via* the oxidative dehydrogenation route. A crucial aspect of catalyst design involves comprehending the role of the metal in the available pathways. Research has indicated that monomeric VO_x demonstrates superior activity compared to species with higher degrees of polymerization in PDH.[31] Conversely, vanadium dimers[32] and polymers have been suggested to be more critical for OPDH, primarily due to the charge transition among two consecutive vanadium atoms. The debate is further complicated by reports of

Table 1 Consecutive and parallel reactions involved in the propylene production

Route	Reaction equations	Mechanism reported
Non-oxidative propane dehydrogenation PDH	$C_3H_8 \rightleftharpoons C_3H_6 + H_2$ (1.1)	Langmuir–Hinshelwood[2]
Sequential reactions of propane dehydrogenation and reverse water gas shift (PDH + RWGS)	$C_3H_8 \rightleftharpoons C_3H_6 + H_2$ (2.1) $CO_2 + H_2 \rightleftharpoons CO + H_2O$ (2.2)	Langmuir–Hinshelwood[2] Mars–Van Krevelen (MVk)
Oxidative propane dehydrogenation	$C_3H_8 + CO_2 \rightleftharpoons C_3H_6 + CO + H_2O$ (3)	Mars–Van Krevelen (MVk)[7]
Oxidative propane dehydrogenation on non-oxidative conditions	$C_3H_8 + O^* \rightleftharpoons C_3H_6 + H_2O + (*)$ (4)	Mars–Van Krevelen (MVk)

O* Oxygen in the lattice. *Vacancy.

anomalous high activity in V_2O_5 nanoparticles on different supports.[33] When discussing vanadium-based dispersion based on the load, some researchers suggest that the transition from individual atoms to more complex structures is directly related to the gradual increase in vanadium loading. However, recent studies using microkinetic models indicate that controlling the formation of diverse VO_x species is not straightforward,[30] leading to the combination of different populations even at low loadings. Essentially, the complex nature of vanadium's role in catalysis is an ongoing topic of discussion and research, with various theories and findings contributing to the complexity of the field. Introducing VO_x species into small-pore zeolites presents unexplored challenges.

Alumina (Al_2O_3) has been successfully utilized in industrial applications as a preferred support material in various processes (*e.g.* Pt–Sn/Al_2O_3 for Oleflex or CrO_x/Al_2O_3 for Catofin[34]) due to its excellent thermal conductivity and stability. Its robust physical properties make it a reliable choice for high-temperature operations.[35] Additionally, VO_x/Al_2O_3 continues to be a subject of extensive research due to its versatility and potential for further improvements.[36–38] However, one of the significant challenges associated with Al_2O_3 is its acidity and prominent porous structure, making it susceptible to rapid deactivation, primarily due to coking. Interestingly, zeolites serve as appealing catalysts within the petrochemical industry due to their capacity to confine active sites, impede coke formation, and enhance catalytic stability.[39] Consequently, a keen interest exists in developing propane conversion and selectivity were high over some of these systems, though only a limited number of frameworks have been tested. Herein, small-pore zeolites, featuring channels bound by rings of at most 8 tetrahedra,[40,41] have gained momentum owing to their recent implementation in processes such as methanol-to-olefin[42–44] and selective catalytic reduction processes.[45–48]

A summary of CHA uses for PDH is presented in Table S1 PDH: for example, Lobo group has focused on Ga- and In/CHA for PDH and ethane dehydrogenation.[49–51] In addition, other metals on CHA were tested; Fu *et al.*[52] show good catalytic performance of Pt promoted by Cu over CHA with a notable 76.5% propane conversion. Remarkably, they revealed a noteworthy correlation between the quantity of coke and acid sites within the catalytic system. Sun *et al.*[53] reported a complete study with V/CHA as a study subject under PDH conditions. It was claimed that nano hierarchical V/CHA revealed suppressed coke deposition, allowing a good mass transfer and accessibility for propane to the active sites. Additionally, reports on catalysts composted by CHA/binder have diminished the gap between the lab-level and industrial application.[54] Aligned to the potential oxidative process, Fu *et al.*[55] demonstrated superior CO_2 adsorption in a CHA structure doped with Zn compared to other framework topologies. Notably, Zn/CHA but with ethane oxidative dehydrogenation has shown nearly equimolar conversion ratios of ethane and CO_2.[56] Despite that, there is scarce

literature on the application of CHA in oxidative dehydrogenation processes.

This paper demonstrates the unexpected performance of vanadium oxides impregnated on small-pore CHA zeolites for CO_2–ODHP. We report on the unique catalytic activity of VO_x (or a cluster thereof) in and on this support and surmise that the V inside the cages of CHA can catalyze the selective production of propylene in high molar rates while simultaneously converting CO_2 to CO. We investigate the characteristics of the catalytic system, the requirements of the host zeolite, and achieve high activity and stability in specifically tailored V/CHA zeolites. The present study frames the observations and discussion within the context of surface engineering and process design. We used time-dependent reactant consumption and product formation comparisons, employing innovative box and whisker analysis.

2. Experimental section

2.1. Catalyst preparation

Alumina (γ-Al_2O_3) was provided by SASOL, Puralox SCCa-5/200, $d_{50} = 100$ μm. The metal salt, NH_4VO_3, as well as oxalic acid were purchased from Sigma-Aldrich. Zeolites CBV720 (ultra-stable Y zeolite, US-Y Si/Al = 15), CBV780 (US-Y, Si/Al = 40), and ZSM-5 (MFI topology, Si/Al = 40) were provided by Zeolyst. The organic structure direct agent (OSDA) for CHA was trimethyladamantyammonium – TMAda - (OH form, 20 wt%, Sachem). The Si sources of LUDOX HS-40 (40%, Sigma-Aldrich) and tetraethyl orthosilicate - TEOS (98%, Merck) were used. $NaAlO_2$ (Fisher Chemicals) and $Al(OH)_3 \cdot 6H_2O$ (Merck) were used as Al sources. Sodium hydroxide and ammonium nitrate were sourced from Fisher Chemicals. Propane in Argon (Air products, 5.000% in Argon 95.000%), propane (Messer, 99.95%), CO_2 (Air Liquide, 99.999%), and N_2 (Air Liquide, 99.999%) were used for the gas-feed composition.

In general terms, the zeolite syntheses were carried out in 23 ml Teflon cups in stainless steel autoclaves (acid digestion vessel 4749, Parr Instruments). The autoclaves were heated in a mechanical convection oven (Heratherm, Thermo Scientific) under 600 rpm internal stirring (heat-resistant multi-position stirring plate, 2 mag) or under tumbling at the corresponding synthesis temperature. After cooling, centrifugation separated the solid phase from its synthesis liquor (6000 rpm, $\geq$5 min, Thermo Fisher Scientific SL16). The samples were washed with deionized water (18.2 MΩ cm^{-1}) until the supernatant showed a pH below 10. The samples were dried overnight at 60 °C before further treatment. Calcination was performed at 550 °C for 5 h at a ramp of 1 °C min^{-1} in a muffle furnace to remove the organic OSDA.

Different Si/Al ratios in CHA composition were obtained based on interzeolite conversion (IZC) starting from USY zeolites.[57–59] The materials were prepared from a mixture of molar proportion $1SiO_2 : 0.025Al : 0.35TMAda : 0.35OH^- : 12.5H_2O$ with the parent zeolite. The syntheses were carried

This journal is © The Royal Society of Chemistry 2025

Catal. Sci. Technol., 2025, **15**, 5295–5317 | **5297**

out for 24 h at 160 °C with stirring. The nominal Si/Al ratio is reported at the end of the catalyst label.

• H-CHA40: proton form of a CHA topology with a final Si/Al ratio (molar) = 40, derived from CBV780 parent.

• H-CHA15: proton form of a CHA topology with a final Si/Al ratio = 15, derived from CBV720 parent.

• H-CHA70: proton form of a CHA topology with a final Si/Al ratio = 70. It was obtained by placing the same starting solution as H-CHA40 into the oven for 1 h at 160 °C and stirring it. The slurry was further cooled, centrifuged, and separated into solid and liquid phases. The supernatant was placed back into the autoclaved and then in the oven under 160 °C for 23 h with stirring.

H-CHA-15-BC: corresponds to a big particle size CHA topology with a Si/Al = 15. This material was produced starting from amorphous sources as LUDOX HS-40 and Al(OH)$_3$.[60] A molar mixture of SiO$_2$:0.08Al$_2$O$_3$:0.3TMAda:0.2NaOH:44H$_2$O was stirred for 6 days at 160 °C. After calcination, the sample was ion-exchanged with 0.1 M solution of ammonium nitrate for 12 h with intermediary steps of washed and dried at 60 °C (ICP-OES indicated the absence of Na cations after exchange). A final calcination was performed at 550 °C for 5 h at a ramp of 1 °C min^{-1}.

Si-CHA-BC: is the pure silicious CHA topology prepared by stirring a solution of TEOS and TMAda until the complete evaporation of ethanol[61] and the partial removal of water (final H$_2$O/SiO$_2$ ratio = 3). Then, HF (40%) was added, and the whole was sealed in an autoclave. The solution was further stirred for 2 days at 160 °C, followed by centrifugation and calcination.

Vanadium pentoxide nanoparticles were prepared based on the work of Asim et al.[62] as a benchmark to highlight the critical role of the support, reaching particle sizes of around 200–600 nm. The final micelle solution was composed of 30 wt% CTAB, 54 wt% 1-hexanol, and 16 wt% of aqueous solution. Two micelle solutions were prepared: 6 g CTAB, 10.8 g 1-hexanol, and 3 g water, which contained 0.2 g ammonium metavanadate, and the second contained 6 g CTAB, 10.8 g 1-hexanol, 3.1 g water, and 0.1 g sulfuric acid. The two solutions were combined after stirring and heated for 3 h at 50 °C. The mixed solution was left to precipitate at room temperature for 2 days. The samples were subsequently washed with water and EtOH and calcined at 400 °C for 2 h in air. Spent material (V$_2$O$_5$ nanoparticles) was analyzed to evaluate the effect of the reaction conditions over small but still bulk vanadium pentoxide.

Incipient wetness impregnation (IWI) was used to load the vanadium precursors into the alumina or zeolites, with a final step of calcination at 600 °C for 5 h at a ramp of 1 °C min^{-1} in a muffle furnace- strong oxidative conditions remove organics from small-pore zeolites post-synthesis (although removal of template at 580 °C is more common), and during IWI, ensuring vanadium remains in its optimal high oxidation state for OPDH. The metal solution volume corresponds to the pore volume of the support. Vanadium IWI solution consists of a mixture of water, NH$_3$VO$_4$ (varying V loading from 0.6 to 5.2 mmol g^{-1}), and oxalic acid (with double the weight amount of NH$_4$VO$_3$ in all the cases). The nominal intended load of vanadium is specified at the start of each label, separated by a backslash to denote the structure, e.g., 0.13 V/CHA40 represents 0.13 mmol$_V$ g$^{-1}_{support}$ in CHA40.

Leaching with citric acid was performed on 1.3 V/CHA70 by exposing the sample to a 0.3 M citric acid solution for 1 hour under agitation (1 g/15 mL solution). The slurry was recovered by centrifugation and subsequently washed with water. The sample was then calcined at 600 °C for 5 hours.

2.2. Catalyst characterization

Elemental analysis was performed using an inductively coupled plasma-atomic emission spectrometer (ICP-AES, PerkinElmer Optima 3300 DV) with signals for V, Si, and Al, at 292.4 nm, 308.2 nm, and 251.6 nm, respectively. Samples were digested in the acid mixture (HF/aqua regia). After a few hours, it was neutralized with 5 mL boric acid solution (0.49 M) and diluted to 20 mL in deionized water. An aliquot was diluted in a nitric acid (HNO$_3$) solution.

The structure and crystallinity of the zeolites were confirmed by X-ray powder diffraction (P-XRD) on a high-throughput STOE STADI P Combi diffractometer in transmission mode with focusing Ge(111) monochromatic X-ray inlet beams (λ = 1.5406 Å, Cu Kα source).

Porosity was measured by nitrogen physisorption (Tristar II 3020, micrometrics) at 77 K on dried samples (16 h at 300 °C under N$_2$). The relative nitrogen pressure varied between 0.01 and 0.99 (P/P_0). The t-plot method (Harkins and Jura) was used to determine the micropore volumes from the adsorption branch. The model of BET analysis was used to determinate the apparent surface area. The BET surface area was determined using a linear fit of the BET equation within the P/P_0 range of 0.05–0.3. The linear fitting yielded an value of 0.99995, and following the recommendations by IUPAC.[63]

The apparent vanadium surface density was estimated as follows:[64,65]

$$\text{Apparent Vanadium Surface density} = \frac{Nv}{S_{BETo}} \quad (1)$$

where Nv is the number of vanadium atoms per gram of catalyst determined by ICP (atoms g^{-1}) and S_{BETo} is the apparent surface area of the catalyst before impregnation (m^2 g^{-1}), leading to a final unit of V$_{(atoms)}$ nm^{-2}.

SEM analysis was performed on the Jeol JSM-6010LV microscope at an acceleration voltage of 15 kV. Zeolite samples were attached to a piece of carbon tape. Subsequently, a thin Pd/Au (60/40 ratio) layer was deposited on the samples to achieve significant conductivity.

TEM samples were prepared by drop-casting a dispersion of the particles on a holey carbon-coated TEM grid (Cu, 300 mesh, Pacific Grid Tech Ltd.). TEM was performed using a JEOL ARM200F microscope operated at 200 kV and equipped with a cold field emission gun (FEG) and a probe aberration

5298 | Catal. Sci. Technol., 2025, 15, 5295–5317

This journal is © The Royal Society of Chemistry 2025

corrector. Energy-dispersive X-ray (EDX) analysis of the samples was performed using a Centurio EDX detector with a large solid angle of 0.98 steradian from a 100 mm^2 detection area.

Temperature-programmed reduction with H_2 (H_2-TPR) and ammonia temperature-programmed desorption (NH_3-TPD) measurements were carried out using an AMI-300 system from Altamira Instruments. For H_2-TPR, the samples (50 mg) were pretreated at 400 °C under N_2 flow to remove adsorbed moisture and impurities. Afterward, the flowing gas stream was switched to ultra-high purity. Upon further cooling to 20 °C, Then a 5% H_2/N_2 flow (25 ml min^{-1}) was flown over the catalyst bed while the temperature was ramped up from 100 to 800 °C at a heating rate of 10 °C min^{-1}. The hydrogen consumption signal was monitored by a thermal conductivity detector (TCD). Before the outlet gases reached the TCD, a cooling trap captured H_2O. The acidity of the samples was determined by ammonia NH_3-TPD using He as carrier gas. Before the tests, the samples were outgassed under a He flow of 25 mL min^{-1} with a heating rate of 10 °C min^{-1} up to 300 °C and kept at this temperature for 30 min. After cooling down to 100 °C, 5%NH_3/He flow of 30 ml min^{-1} was brought through the sample for 45 min (considered enough for saturation). The samples were flushed by flowing He at 100 °C for 5 min to remove gas-phase NH_3 molecules. Subsequently, the surface acidity was determined by measuring the amount of desorbed ammonia during the gradual temperature increase up to 700 °C with a heating rate of 10 °C min^{-1}. The ammonia concentration in the effluent helium stream was measured with a thermal conductivity detector (TCD). Experiments conducted with helium in the absence of NH_3 revealed a peak above 550 °C, corresponding to surface dihydroxylation. Therefore, these peaks were excluded from the acidity determination.

X-ray photoelectron spectroscopy (XPS) analyses were conducted at room temperature using an SSI-X-probe (SSX 100/206) photoelectron spectrometer manufactured by Surface Science Instruments (USA). The spectrometer was equipped with a monochromatic Al K X-ray microfocused source (1486.6 eV). For sample preparation, the specimens were fixed to small sample holders using adhesive tape and positioned on an insulating ceramic carousel made of Macor® from Switzerland. To mitigate charge effects, a nickel grid was placed over the samples, and a flood gun set at 8 eV was employed. Calibration of the binding energy scale was accomplished by aligning the Si 2p peak at 103.5 eV as a reference.[66] Data processing was executed using the CasaXPS program developed by Casa Software Ltd. (UK). The spectral peaks were deconvoluted into a combination of Gaussian and Lorentzian functions (with an 85/15 ratio) following the subtraction of a Shirley-type baseline.

We measured the weight loss of the spent catalysts with thermogravimetry analysis (TGA/DSC 3+, mettler toledo), following a N_2/O_2 temperature ramp to discriminate between water, soft coke, and hard coke contributions. Water desorption accounts for the weight drop during a ramp from room temperature to 200 °C at 10 °C min^{-1} under a flow of N_2 (90 mL min^{-1}) and an isotherm for 10 min. The subsequent weight drop is attributed to soft coke and occurs when raising the temperature from 200 to 600 °C at 5 °C min^{-1}, always under N_2 flow. The estimated amount of hard coke corresponds to the final variation in weight where, under isothermal conditions at 600 °C, the gas-flow is switched from N_2 to O_2 for 30 min.

2.3. CO$_2$-ODHP reaction

The catalysts were pressed and sieved to 125–250 μm to avoid internal mass transfer and temperature gradient limitations. The reactor comprises a packed-bed hastelloy-x reactor (ID 3.5 mm) loaded with 0.200 ± 0.002 g of catalyst. The bed was diluted with SiC (350 μm) in the isothermic central zone, and 4 grams of SiC was also added below and above the catalytic layer (see Scheme S1). After the reaction, the reactor content was sieved to recover the spent catalyst from the SiC for further analysis. A Thermo Scientific Trace 1300 GC, with a TCD detector (Haysep N 60–80 0.25 m, Rt-XL Sulfur 60–80 1 m, Molsieve 5 Å 60–80 2 m, He carrier) and a FID (CP-PoraPLOT Q 25 m, He carrier) analyzed the absolute gas composition using N_2 as an internal standard to calculate the outlet flowrate. Water and coke formation were derived from oxygen and carbon molar balances and reported in terms of molar flow rates.

In a standard catalytic test, 100 Nml min^{-1} (normal conditions defined at 1 atm, 0 °C) of the gas mixture flow $CO_2/C_3H_8/Ar/N_2$ (2.5/2.5/45/50) was fed. Before catalytic testing, an activation procedure was followed, raising the temperature from room temperature to 600 °C at 1 °C min^{-1} at 6 bar. (GHSV = 3.0 × 10^4 Nml ml$_{cat}^{-1}$ h^{-1}, WHSV = 1.5 g$_{propane}$ g$_{cat}^{-1}$ h^{-1}, 1.5 g$_{CO_2}$ g$_{cat}^{-1}$ h^{-1}). The next three steps were isothermal time on stream (TOS) reactions. The first is classical PDH conducted at 6 bar. The last two stages were OPDH conducted at 0.6 and 6 bar. Between each step, the catalyst was regenerated by air (10 ml min^{-1}, 60 min) at 600 °C.

To calculate the consumption rates of reactants and the production rates of main and side compounds, the N_2 flow was used as an internal standard. Additionally, the next equations define our use of conversion of component i (X_i), selectivity for component j (S_j), yield of propylene ($Y_{C_3H_6}$) and space time yield of propylene ($STY_{C_3H_6}$):

$$X_i = \frac{F_i^{IN} - F_i^{OUT}}{F_i^{IN}} \tag{2}$$

$$S_j^{HC} = \frac{\vartheta_j F_j^{OUT}}{\sum_j^{HC} \vartheta_j F_j^{OUT}} \tag{3}$$

$$Y_{C_3H_6} = \frac{F_{C_3H_6}^{OUT}}{F_{C_3H_8}^{IN}} \tag{4}$$

$$\text{STY}_{C_3H_6} = r_{C_3H_6} = \frac{F_{C_3H_6}^{OUT}}{w} \quad (5)$$

where F_i is the molar flow of i at the reactor (IN) and outlet (OUT) inlet, measured during the reaction in mol h^{-1}, r is reaction rate in mol h^{-1} kg$_{cat}^{-1}$, and w is mass of catalyst in kg.

Given the presence of multiple reactions, including coke formation and propane dry reforming, we define the reaction's propane selectivity based on a carbon atom basis. There, dry reforming, $F_{CO}^{OUT} \geq F_{CO_2}^{IN} - F_{CO_2}^{OUT}$ and some other reactions have $S_{CO} = F_{CO}^{OUT}/\left(F_{CO_2}^{IN} - F_{CO_2}^{OUT}\right) > 1$. We therefore distinguish the source of CO by the molar balance between propane and CO$_2$: $F_{CO}^{\text{from propane}} = F_{CO}^{OUT} - \left(F_{CO_2}^{IN} - F_{CO_2}^{OUT}\right)$ and $F_{CO}^{\text{from } CO_2} = F_{CO_2}^{IN} - F_{CO_2}^{OUT}$ and we define:

$$S_{\text{reaction}}^{\text{propane}} = \frac{\text{reaction}}{\sum_j^{HC} \vartheta_j F_j^{OUT} + F_{CO}^{\text{from propane}} + F_{\text{coke}}} \quad (6)$$

where $S_{\text{reaction}}^{\text{propane}}$ is the overall selectivity of propane towards the "reaction" = (O)DHP = $3F_{C_3H_6}^{OUT}$ "oxidative" is in parenthesis as we cannot infer the route (direct or indirect); cracking = $F_{CH_4}^{OUT} + 2F_{C_2H_4}^{OUT}$, reforming = $F_{CO}^{\text{from propane}}$, coking = F_{coke} and all the remaining j species as "others" = $\sum_{j'}^{NC} \vartheta_{j'} F_{j'}^{OUT}$ (hydrogenation of ethylene to ethane, cyclization or propane, propyne, propadiene, 1,3-butadiene, and other C$_4$ HC). F_{coke} is derived from the deficit in the C-mass balance.

Catalytic profiles of the materials, depending on the chemical species as rates consumed or produced, were plotted in the interquartile analysis, also known as a box plot. This graphical representation displays the distribution of profile data, highlighting measures of central tendency (average) and the rates range covered in the time of the experiment. In a box plot, a rectangle (the "box") is drawn to cover the interquartile range of profile (IQR) between the first and third quartiles of the experiment. Within the box, a line (−) is plotted to represent the median. Then, "whiskers" (labeled as **o** and **▼**) extend from the box to the extreme values, pointing to the initial (**o**) and final value (**▼**). In the context of our study, interquartile analysis serves to partition the experiment's activity into distinct segments, with the interpretation differing according to the test conditions. For TOS experiments, each interquartile signifies the material's activity over a 50-minute timeframe (1/4 of total TOS at 600 °C) (further information is found in Fig. S1 and S2).

Residual activity (α)[67,68] is a dimensionless factor between 1 and zero, which is the ratio of the activity at time i over the initial activity. Initial activity corresponds to 1, and complete deactivation is equivalent to 0.

$$\alpha = \frac{r_i}{r_o} \quad (7)$$

Individual experiments were conducted on blanks for SiC, CHA40, and V$_2$O$_5$ nanoparticles to ensure the accuracy of the conclusions regarding activity in the sample sets (see Fig. S3 and S4).

3. Results and discussion

3.1. Pristine zeolites characterization (before impregnation)

3.2. Analysis of surface characteristics and acidity for materials with 1.3 mmol g^{-1} vanadium

Custom CHA zeolites were made with different particle sizes and Al content, giving a Si/Al ratio ranging from 13 to ∞ (pure silica), as measured with ICP. As materials with particle sizes bigger than 1 μm have poor activity and fast deactivation (see Fig. S5 and S6), CHA with particle size below 0.5 μm were selected for further study (Table 1). The XRD patterns confirm the purity of the CHA phases (Fig. S15). All the synthesized zeolites presented isotherm type I[63] and a micropore volume of around 0.3 cm^3 g^{-1}, which is typical for SSZ-13 of the CHA family. The morphology of the materials was checked with SEM, where, H-CHA40 and H-CHA70 show regular crystal shapes in accordance with the expected CHA morphology made *via* this route.[58] H-CHA15 recurrently comprised particle aggregation; however, an inspection of individual particles revealed a regular cubic shape.[59] (Fig. S20).

Acidity determined using NH$_3$-TPD, showed a progressive decrease in the total acid with the increase in the Si/Al ratio of the zeolites (Table 2) from 1287 to 475 μmol g^{-1}, meanwhile the acid density follow 1.9–1.0 μmol m^{-2}. In the case of H-CHA15, two distinct peaks are observable in the temperature ranges of 185–250 °C and 440–475 °C. Contrarily, both H-CHA40 and H-CHA70 exhibit an additional third signal appearing above 600 °C, attributed to surface dehydroxylation. This is confirmed by the presence of the same peak in equivalent acidity determination experiments without NH$_3$, indicating the removal of surface hydroxyl groups at high temperatures. Traditionally, NH$_3$ desorption signals below 250 °C are attributed to NH$_3$ species on weak acid sites or to physically stacked NH$_3$ in the pores of the zeolite. Above this threshold, a gradual increase in the acidity strength is presumed, highlighting stronger acid sites on H-CHA40 and H-CHA70 than H-CHA15. Several vanadium loadings were performed on the studied zeolites, covering the range from 0.13 to 5.2 mmol V g$_{zeolite}^{-1}$ (Table 2), corresponding to a vanadium apparent density of 0.2–3.4 V$_{atoms}$ nm^{-2}. Overall, the increase in vanadium loading was directly proportional to the reduction in the micropore volumes and the apparent surface areas of the zeolites.

We chose a nominal vanadium load of 1.3 mmol g^{-1}, corresponding to surface densities of less than <2 V$_{atom}$

5300 | *Catal. Sci. Technol.*, 2025, **15**, 5295–5317

This journal is © The Royal Society of Chemistry 2025

Table 2 List of the studied materials in this work and their structural and textural properties. NH$_3$-TPD analysis were only carried out for a selection of materials

Materials	Micropore volume[a] cm^3 g^{-1}	BET apparent surface[a] m^2 g^{-1}	V load ICP-AES mmol g^{-1}	% V w/w	Vanadium apparent density V_{atoms}[b] nm^{-2}	Particle size[c] (μm)	Total acidity NH$_3$-TPD – μmol[d] g^{-1}) (acid density – μmol[e] m^{-2})
CHA15	**0.31**	**669**	**0**	**0**	**0.0**	**0.5–1 μm**	**1278 (1.9)**
0.13 V/CHA15	0.28	617	0.15	0.76	0.1		
0.65 V/CHA15	0.28	590	0.68	3.4	0.6		
1.3 V/CHA15	0.19	395	1.20	6.1	1.1		1214[f] (3.0)
2.6 V/CHA15	0.09	205	2.0	10.2	1.8		
5.2 V/CHA15	0.02	27	3.4	17.3	3.1		
CHA40	**0.31**	**591**	**0**	**0**	**0.0**	**0.5–1 μm**	**755 (1.2)**
0.13 V/CHA40	0.28	492	0.11	0.56	0.1		
0.65 V/CHA40	0.28	475	0.64	3.2	0.7		
1.3 V/CHA40	0.16	310	1.1	5.6	1.1		
2.6 V/CHA40	0.08	156	1.7	8.4	1.7		
5.2 V/CHA40	0.01	29	3.8	19.4	3.4		
CHA70	**0.28**	**468**	**0**	**0**	**0.0**	**<0.2 μm**	**475 (1.0)**
1.3 V/CHA70	0.23	393	1.19	6.1	1.5		
1.3 V/Al$_2$O$_3$	0.002	199	1.30	6.6	3.9		—

The bold and italic fonts point to the pristine materials without vanadium deposited. [a] The materials show Isotherms type I (see Fig. S16). [b] The values below 1 atom per nm^2 represent a statistical average density, indicating very low dispersion (high distance between individual atoms or clusters). [c] Evaluated by SEM. See Fig. S20. [d] Not *per se* only aluminum-derived. For more details about NH$_3$-TPD see F16–17 and Table S1. Note: above 650 °C, signals may be biased due to NH$_3$ decomposition and dihydroxylation. [e] Acid density refers to the apparent surface area of each catalyst. [f] 1.3 V/CHA15 to evaluate the effect of impregnation on the acidity.

nm^{-2} (<8–10 V_{atom} nm^{-2} in Al$_2$O$_3$ (ref. 33, 36, 38)) to evaluate the direct impact of the resulting acidity, metal dispersion, and to compare the zeolites' catalytic performance with our (industrial) benchmark support, Al$_2$O$_3$. Likely, the comparison is estimated under sub-monolayer conditions with a narrower V-speciation.[7]

From the zeolite set, H-CHA15 presented the highest acid density as revealed by NH$_3$-TPD analysis, which renders it a good model to follow acidity changes before and after the impregnation step (Fig. 1A). Despite the metal load of 1.3 mmol$_V$ g^{-1}$_{support}$ (actual 1.2 mmol$_V$ g^{-1}$_{support}$) being expected to result in more vanadium atoms than acid sites (Table 2), only modest changes in the NH$_3$ desorption profile were observed above 300 °C and the total acid density slightly decreased from 1278 μmol g^{-1}$_{naked}$ to 1214 μmol g^{-1}$_{catalyst}$. Notably, the inclusion of metal caused a reduction in apparent surface area without affecting the total acidity. This combination led to an increase in acid site density, shifting the value from 1.9 to 3.0 μmol m^{-2}. V/CHA15 with bigger crystal showed similar results in the acidity changes after impregnation (see Fig. S18).

Fig. 1C compares the STEM images with elemental mapping for 1.3 V/CHA15, 1.3 V/CHA40, and 1.3 V/CHA70. The intensity corresponding to bulk elements (Si, Al, and O) contrasted with vanadium (purple), which indicates whether vanadium is agglomerated or well dispersed on the zeolite. The V/CHA15 sample reveals more prominent aggregates than the other samples, with aggregates of around 10 nm. V/CHA40 shows an intense contrast of vanadium at the crystal edges compared to the mapping of the bulk elements. The smallest crystallite size of V/CHA70 appears

to result in a more uniformly dispersed vanadium with an overall enhanced homogeneity.

H$_2$-TPR was performed to provide additional insights (Fig. 1B), where next to the zeolite samples, V$_2$O$_5$ and 1.3 V/Al$_2$O$_3$ were tested as reference materials. Since the reduction kinetics of vanadium exhibit a wide range of vanadium states and polymerization degrees, the correlation between the H$_2$-uptake or the peak reduction temperature on the one hand and the state of vanadium, on the other hand, cannot be directly made.[70] However, sharp peaks in the 450–550 °C range are often associated with less complex species of VO$_x$ species bonded to the zeolite. Conversely, for less reducible polymers, the literature indicates that the reduction peak tends to shift toward higher temperatures.[31] With a single reduction peak around 493 °C, 1.3 V/Al$_2$O$_3$ shows a prominent reduction. 1.3 V/CHA15 has a single peak with a maximum temperature of 545 °C and a shoulder at 565 °C. 1.3 V/CHA40 presents the most complex profile with three peaks (531, 589, and 628 °C) and a small shoulder at high temperatures (around 670 °C). Two peaks are found in the 1.3 V/CHA70 reduction profile: a sharp peak around 544 °C (shoulder around 571 °C) and a small peak at 652 °C. While care should be taken not to overinterpret these TPR profiles, it is clear that the V supported in and on small-pore zeolite CHA samples is more difficult to reduce than on the non-microporous γ-Al$_2$O$_3$ benchmark (in materials under monolayer formation). We surmise that vanadium located in the inner layers of the crystal in CHA systems needs harder reduction conditions, resulting in complex TPR profiles. As the nature of metal atoms located in the external surface is not the same that those in deeper layers of micropores, this
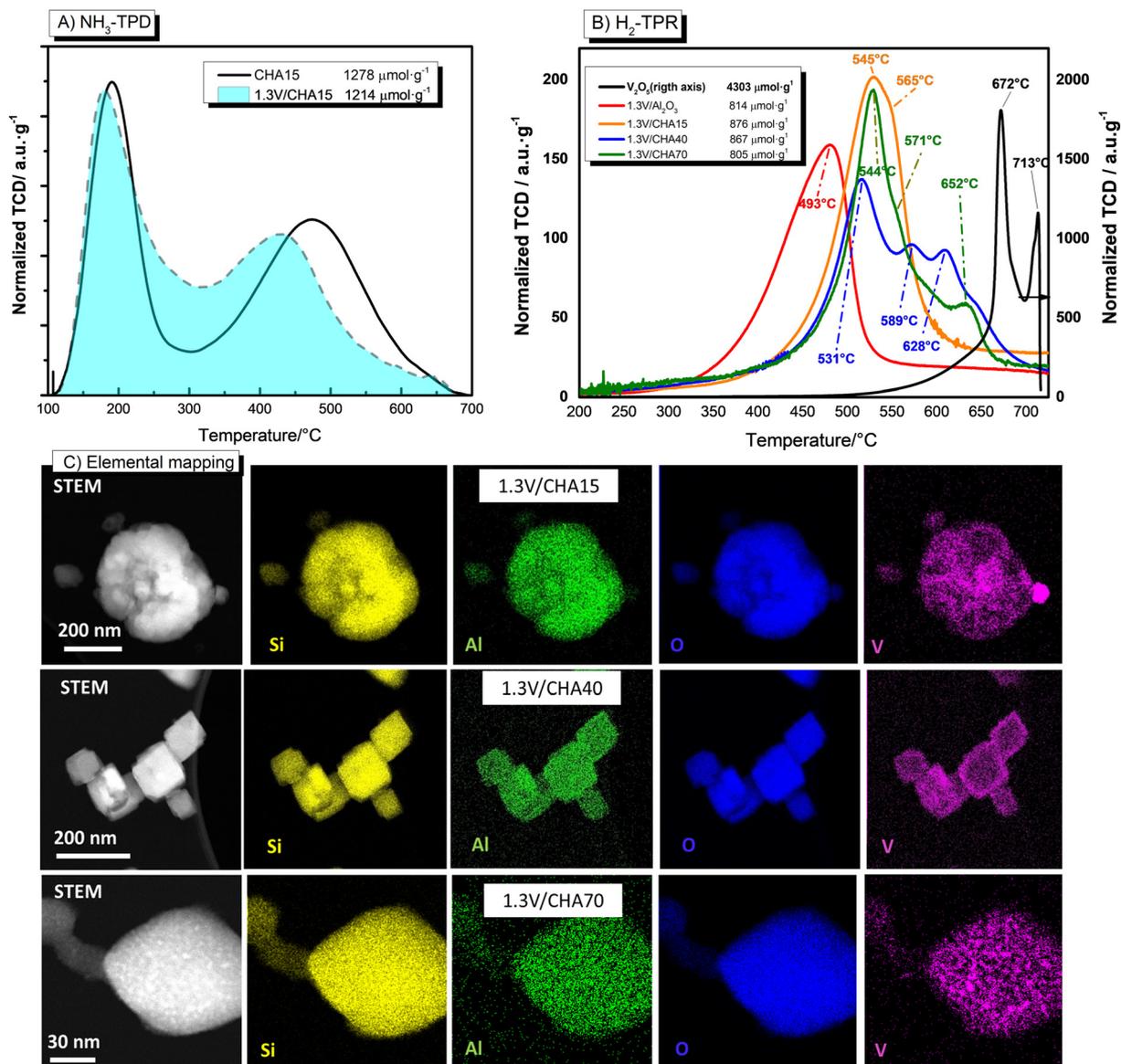
Fig. 1 A) NH_3-TPD comparison of CHA15 zeolite support before and after the impregnation of 1.3 mmol g^{-1} vanadium. B) H_2-TPR profiles for the zeolites (left-hand axis) and for bulk V_2O_5 (right-hand axis). C) STEM images and elemental EDS mapping (Si, Al, O, and V) for 1.3 V/CHA15, 1.3VCHA40, and V.3VCHA70.

result encourages optimization of synthesis (and V impregnation) parameters as potential strategy for catalyst improvement.

Considering that molar H_2-uptakes are below the molar vanadium loading (*ca.* 1.3 mmol g^{-1}, see Table S2) and measured on samples that underwent on oxidative conditions during calcination, through the metal impregnation procedure (air calcination), it is likely that the primary state transition in TPR corresponds to V^{+5} being reduced to V^{+4}. This estimation is complicated due to the accessibility of the metal. The presence of a small population of species reaching V^{+3} cannot be entirely ruled out.

It is reported that XPS analysis over vanadium modifies the oxidation state of metal (*e.g.*, reduction under vacuum or flood gun), so care must be taken in interpreting the

results.[71–73] In this study, the V $2p_{3/2}$ XPS signals were decomposed into two distinct peaks at around 517.5 eV, and 516.5 eV, respectively, assigned to V^{5+} and V^{4+} (Table S3). The presence of various V species is in line with the results of the H_2-TPR measurements. Despite the oxidative environment during metal/zeolite preparation (600 °C, 8 hours) not all vanadium is in the V^{5+} state. This observation has also been previously reported in the literature.[71,74,75] Specifically for CHA structure, changes in the species population were reported with dependency on the vanadium load.[53] For the 1.3 V/CHA40 sample, 75% of the vanadium highest oxidation states (+5) in the fresh catalyst, which decreased to 61% in the spent material. The 1.3 V/CHA70 sample showed a similar trend, starting at 66%, but the reduction degree of the V-population increases, with the occurrence of V^{5+} species

5302 | *Catal. Sci. Technol.*, 2025, **15**, 5295–5317

This journal is © The Royal Society of Chemistry 2025

decreasing to 25% after use. In-depth, 1.3-V/CHA70 shows the strongest reduction compared with the equivalent sample, 1.3 V/CHA40, after the reaction.

Furthermore, given the surface depth in the analysis (~3 nm), the V/Si ratio compared to bulk analysis (ICP) provides additional evidence to support the discussion. The 1.3 V/CHA40 sample exhibits a V/Si ratio of 0.08 in bulk, which is lower than the XPS value of 0.19. Conversely, the 1.3 V/CHA70 sample shows a bulk ratio of 0.09, with a lower apparent surface value of 0.04. These findings indicate a more effective dispersion in the 1.3 V/CHA70 sample, characterized by smaller crystal size and reduced aluminum content.

3.3. Catalytic screening at different aluminum content and benchmarking

Benchmark catalytic tests for the naked support of CHA40 and pure V_2O_5 nanoparticles (see Fig. S3 and S4) showed a negligible conversion and fast deactivation.

The catalytic performances of the zeolite catalysts were analyzed and compared to 1.3 V/Al_2O_3. Fig. 2A depicts the conversion/selectivity and production and conversion rates, averaged from the TOS experiment, while Fig. 2B shows a box and whisker analysis applied to the 200-minute time-on-stream rate data of reactants and selected products (equivalence of approximate conversions compared with consumption rates of reactants is shown in the small inset). Carter et al.[76] pointed out that the propane to propylene selectivity can be biased by artefacts in the estimation method, so for an even more accurate representation, Fig. 2C displays the consumed propane on the x-axis and the produced propylene on the y-axis. The diagonal indicates the ideal case for a selective conversion from propane to propylene in a molar ratio of 1.

The box and whisker is to be read as follows (as detailed in our previous work[15]): the beginning of catalytic profile is the dot, then one should follow the whisker down as a vertical time on stream, to the start of the box (rate at 50 minutes), the line at 100 minutes, the end of the box at 150 min, and finally to the arrow, which is the end of the profile
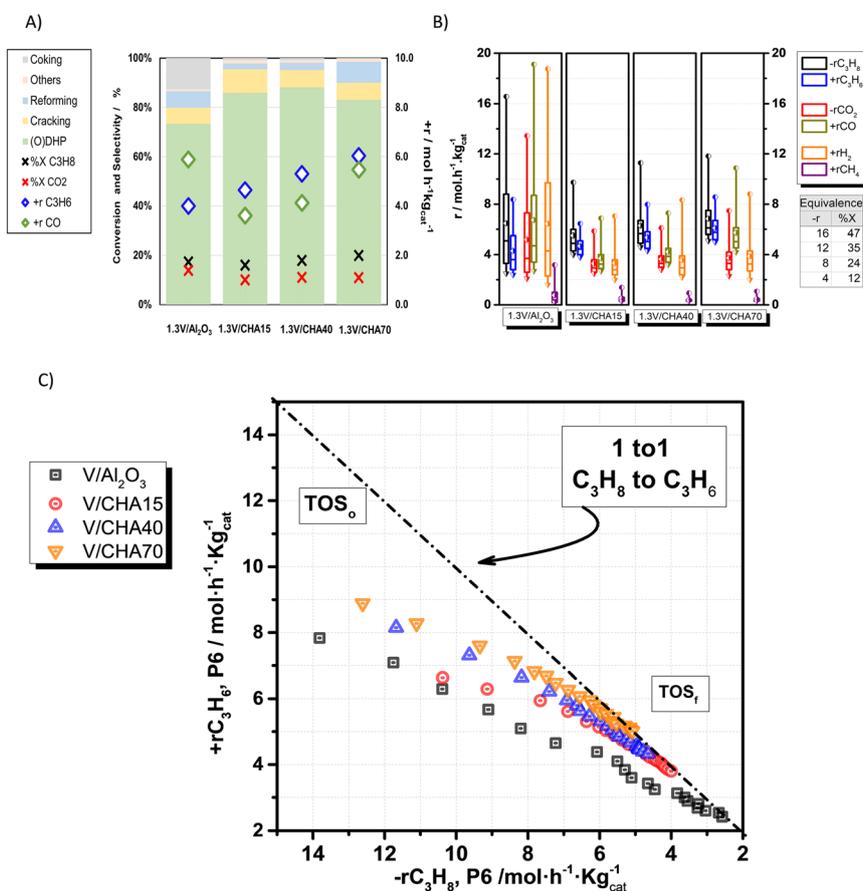
Fig. 2 A) Conversion and selectivity (left axis) and product rates (right axis) averaged during TOS stage reactions over 1.3 V/Al_2O_3, 1.3 V/CHA15, 1.3 V/CHA40, and 1.3 V/CHA70. B) Box and whisker analysis for ODHP reactions over 1.3 V/Al_2O_3, 1.3 V/CHA15, 1.3 V/CHA40, and 1.3 V/CHA70. Small inset displays the equivalence between reactant rate consumed and approximate conversion. C) Propylene production vs. propane consumption rates. Reactions were performed at 600 °C under 6 barg pressure and gas ratios of $CO_2/C_3H_8/Ar/N_2$ = 2.5/2.5/47.5/47.5 Nml min⁻¹, WHSV 1.5 $g_{C_3H_8}$ g_{cat}^{-1} h⁻¹. The total time on stream (TOS) duration was 200 minutes, with product sampling conducted every 10 minutes. Subscripts o and f in TOS indicate the profile at time zero and 200 min respectively.

at 200 min. Note that the diamond is the time-averaged rate over 200 min. The box and whiskers analysis method in Fig. 2B makes it easy to show non-overlapping rates and deactivation profiles all in one, *i.e.* of propane consumed to propylene yielded, CO_2 consumed to CO produced, and hydrogen and methane produced at 600 °C and 6 barg. 1.3 V/Al_2O_3 exhibited the highest initial hydrogen and CO production and a decent propylene production rate (second among the tested materials). Notably, by the end of the experiment, this material showed lower activity than the zeolite-based catalysts, indicating its higher (and faster) deactivation. For the zeolite series, interestingly, the propylene production appears to be enhanced with the lowering of the aluminum content (Si/Al = 15, 40, and 70), although the particle sizes are also becoming smaller in low-aluminum zeolites (from 0.5 μm to below 0.2 μm). The methane formation -which indicates propane cracking- was the highest on the 1.3 V/Al_2O_3 catalyst. In the zeolites series, the evolution of the methane formation does not seem to follow the evolution in the Si/Al ratio nor the particle size, as similar results were observed for both 1.3 V/CHA15 and 1.3 V/CHA70.

The production of H_2 occurs through PDH and deep dehydrogenation (coke formation); mitigation of both pathways is required if the goal is to transition to OPDH and avoid frequent regeneration (industrial requirement). A third possible path to H_2 production is the dry reforming of propane, which produces 4 H_2 for one propane, which is believed to have a minor contribution. In this sense, hydrogen's first quartile for 1.3 V/Al_2O_3 (orange top whisker, first 50 minutes) is much higher and longer than for the V/CHA catalysts. At the same time, this contrasts with the lowest hydrogen production at the end of the experiment for the same material (lowest arrow point). So, this, along with the selectivity shown in form of the green area in Fig. 2A, suggests vanadium on the surface of the 1.3 V/Al_2O_3 catalyst produced propylene but also other olefinic and (possibly aromatic) polymers, which covers the active site leading to fast deactivation.

The well-organized small pore system in CHA supports handles OPDH more efficiently than alumina. First, the propylene rate was higher than the other products. Second, the selectivity in the conversion from propane to propylene was high, and this is clear through the high match of the propane profile with the propylene production profile, coking is minimal, unlike in V/Al_2O_3 where 10% of the feed material is lost this way. For V/Al_2O_3 additionally this increases CO rates due to the subsequent reverse Boudouard CO_2-dry reforming of coke. The selectivity differences are also evident in Fig. 2A. And third, if we plot rates of propane consumption *vs.* propylene production in Fig. 2C, we observe that the 1.3 V/Al_2O_3 performance remains further from the ideal 1:1 conversion (diagonal line), whereas the series of zeolites are closer to that parity line. CHA70 exhibited the highest average propylene production rate, indicating a more efficient conversion process (also in Fig. 2A). Fig. 2C also

confirms that V/CHA70 (represented by yellow triangles) is closest to the ideal selective conversion of propane to propylene. It is likely that at the beginning of the reaction (TOS_0), the abundance of rich-O-sites allows for a different transient mechanism *vs.* the reaction after longer TOS, in which we can assume a pseudo steady state and equilibrium between the various species and intermediates populating the catalyst's surface is reached. The average propylene production is higher for all V/CHAs due to their combined activity and selectivity. Specifically, 1.3 V/CHA70 offers a 50% higher propylene space-time yield than 1.3 V/Al_2O_3.
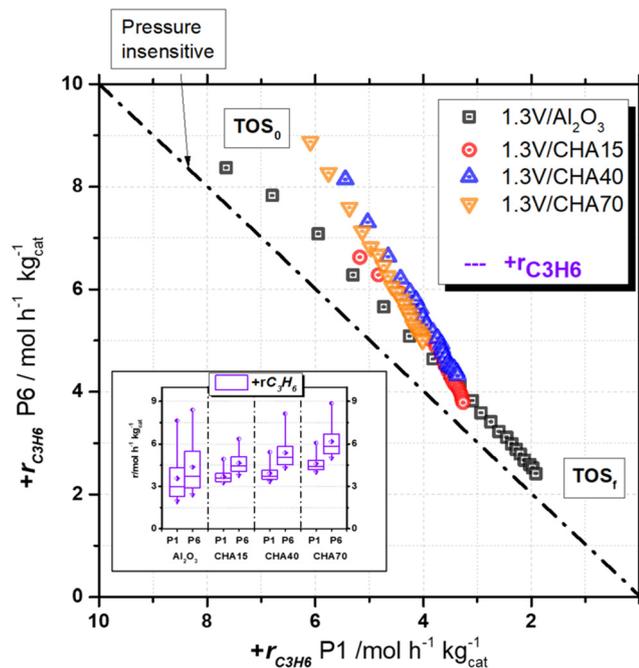
Finally, despite that the CO_2 consumed on average was the highest for 1.3 V/Al_2O_3, the fast deactivation seen in all its box and whisker profiles leads to the lowest CO_2 consumption rate after 200 min (near total deactivation). On top, a decent part of the CO_2 conversion in the alumina comes from dry reforming (3 CO_2 are consumed there for each propane reformed, which leads to 6 CO and 4 H_2), which explains the higher CO production *versus* CO_2 consumption. For the small pore materials, the conversion of CO_2 to CO is more selective, reaffirming few dry reforming, and a significant fraction of CO_2 to CO from the OPDH reaction.

In the context of the previous discussion concerning kinetic reducibility (H_2-TPR), these preliminary findings point out a moderate range of reducibility temperatures (520–590 °C), and perhaps this is linked to the vanadium oxide redox cycles demonstrating enhanced activity for OPDH. In reverse, the facile reducibility observed for the V/Al_2O_3, with a reduction peak fully below 520 °C could potentially account for the rapid formation of lower oxidation states in the reaction, thereby enhancing (or indicating) coke (polymer) formation and dry reforming reactions dominant over (O) PDH and propylene selectivity.

3.4. Catalytic performance shift due to pressure sensitivity

The standard catalytic test involved assessments conducted at two different pressures (after a ramp and PDH stage, see section 2.3): first, a stage in atmospheric conditions (reaching 1 barg with a delta of pressure around 0.3 barg) and secondly, under imposing a restriction of 6 barg, both with negligible pressure drop across catalyst bed(around 0.3 barg). The catalyst underwent an *in situ* regeneration under air between the two pressure reaction stages. Changes in total system pressure significantly influence catalytic activity by impacting both chemical and physical equilibria, which vary depending on the specific reaction pathway involved. Elevated pressures enhance the concentration of molecules confined within catalyst pores and increase surface adsorbed species. Consequently, reactions with higher molecularity and polymerization tendencies could be favoured, highlighting the crucial role of the support and its pores in influencing local concentrations (mass transfer). However, all these factors complicate predictions solely based on reaction

5304 | *Catal. Sci. Technol.*, 2025, **15**, 5295–5317

This journal is © The Royal Society of Chemistry 2025

Fig. 3 Pressure effect over V supported on Al_2O_3, CHA15, CHA40 and CHA70 zeolites with a nominal load of 1.3 mmol g $_{support}^{-1}$. The analysis shows propylene produced at P1 = 1 barg (x-axis) and P6 = 6 barg (y-axis). A pressure insensitive diagonal is shown as a dashed line. $TOS_0 = 0$ and $TOS_f = 200$ min. Small inset is propylene production rate, all of them for 1 and 6 barg displayed by box and whisker analysis. Reaction conditions: 600 °C using gas ratios of $CO_2/C_3H_8/Ar/N_2 = 2.5/2.5/47.5/47.5$ Nml min^{-1}, GHSV 3.0×10^4 Nml gas ml_{cat}^{-1} h^{-1}, and WHSV 1.5 $g_{C_3H_8}$ g_{cat}^{-1} h^{-1}. The effect of slightly varying GC sampling times was corrected through interpolation of the experimental data. The total time on stream (TOS) duration was 200 minutes, with product sampling conducted every 10 minutes. See Fig. S13 pressure effect over propane consumption rate, CO_2 consumption rate and propylene production.

molecularity, and beforehand, conclusions are not straightforward based on the reaction network.

Fig. 3 addresses the complex interpretation of the catalytic system as follows: box and whisker analysis was performed for propane, CO_2, and propylene, as shown in Fig. S13A, B and C, respectively. This analysis highlights the comparison between Al_2O_3 and CHAs, emphasizing activity shifts due to the imposed pressure in the system. Additionally, Fig. 3 displays propylene production at low pressure on the x-axis and propylene production at high pressure on the y-axis, with both values corrected by interpolating experimental data (slightly varying sampling timings) to equal times. In this plot, stamps TOS_o and TOS_f indicate the direction of reaction advance from top left to bottom right. Furthermore, we define the pressure-insensitive line as a hypothetical scenario where the propylene production remains constant despite imposed pressure changes on the system and it is shown as a diagonal dash-dot line.

The behavior of propylene production with pressure is quite different from that of the reactants (see Fig. S13). On average, zeolites outperformed Al_2O_3 at 6 barg, as the

pressure-induced changes were more significant than those observed for the reactants. For example, zeolites displayed average values of 4.6, 5.4, and 6.2 mol$_{propylene}$ h^{-1} kg$_{cat}^{-1}$ for 1.3 V/CHA15, 1.3 V/CHA40, and 1.3 V/CHA70, respectively, surpassing the value of 3.5 mol h^{-1} kg$_{cat}^{-1}$ recorded for V/Al_2O_3 at high pressure. This was also reflected in the final value of the TOS (arrowhead at the bottom at the small inset Fig. 3).

Fig. 3 compares propylene production at high and low pressure. The diagonal line indicates a pressure insensitive performance and a slope of 1. The zeolites behave quite different than the alumina: the distance from the diagonal is quite large for zeolites at initial TOS, but the gap decreases with reaction advancement (moving down toward TOS_f, bottom right). The slope of the profiles tended to be quite constant but differing for each material. The slopes in Fig. 3 are −1.1, −1.5, −1.8, and −1.9 for 1.3 V/Al_2O_3, 1.3 V/CHA15, 1.3 V/CHA40, and 1.3 V/CHA70, respectively. One could argue that the narrowing of the gap (getting closer to 1) and thus the decrease in pressure sensitivity is linked to the deactivation of the most active sites and that in the case of the superior zeolite materials (1.3 V/CHA70 e.g.) these sites are more sensitive to pressure effects in their mechanism (linked to their kinetics) than the sites at work in 1.3 V/Al_2O_3. In the end, with all catalysts behaving quite similar in term of pressure response at a certain lower rate (longer TOS points, Fig. 3), one could hypothesize that the sites remaining at work there are less kinetically influenced by the pressure (and thus the partial pressures of reagents). These less active sites (or sites that are still working in the later TOS regime) could be more similar across different catalysts.

The above analyses underscore a compelling trend. The CHA materials (especially the low Al-content one) showcase remarkable stability, selectivity and OPDH-favorable sensitivity to pressure alterations, signaling a distinct advantage over the conventional counterparts (Al_2O_3) commonly found in classical PDH methodologies. Moreover, this observation positions pressure as a beneficial variable for optimization, even though the thermodynamic equilibrium (not reached here) would be a bit lower for higher pressures. Operating at higher pressure could be beneficial industrially in concentrating streams or avoiding recompression costs.

3.5. Modulating surface vanadium density for the ODHP reaction

The dependency on monomers, polymers, and monolayer formation is proportional to vanadium load increments. However, regions dominated by monomers are not entirely excluded from forming more complex species and vice versa. The formation of a monolayer has been reported and established in non-microporous materials with an apparent vanadium density ranging from 2 to 10 V atoms nm^{-2} (e.g., Ceria,[77] Al_2O_3, Zirconia,[78] TiO_2, or SiO_2 (ref. 33, 79, 80)). This approach must be carefully handled when extended to
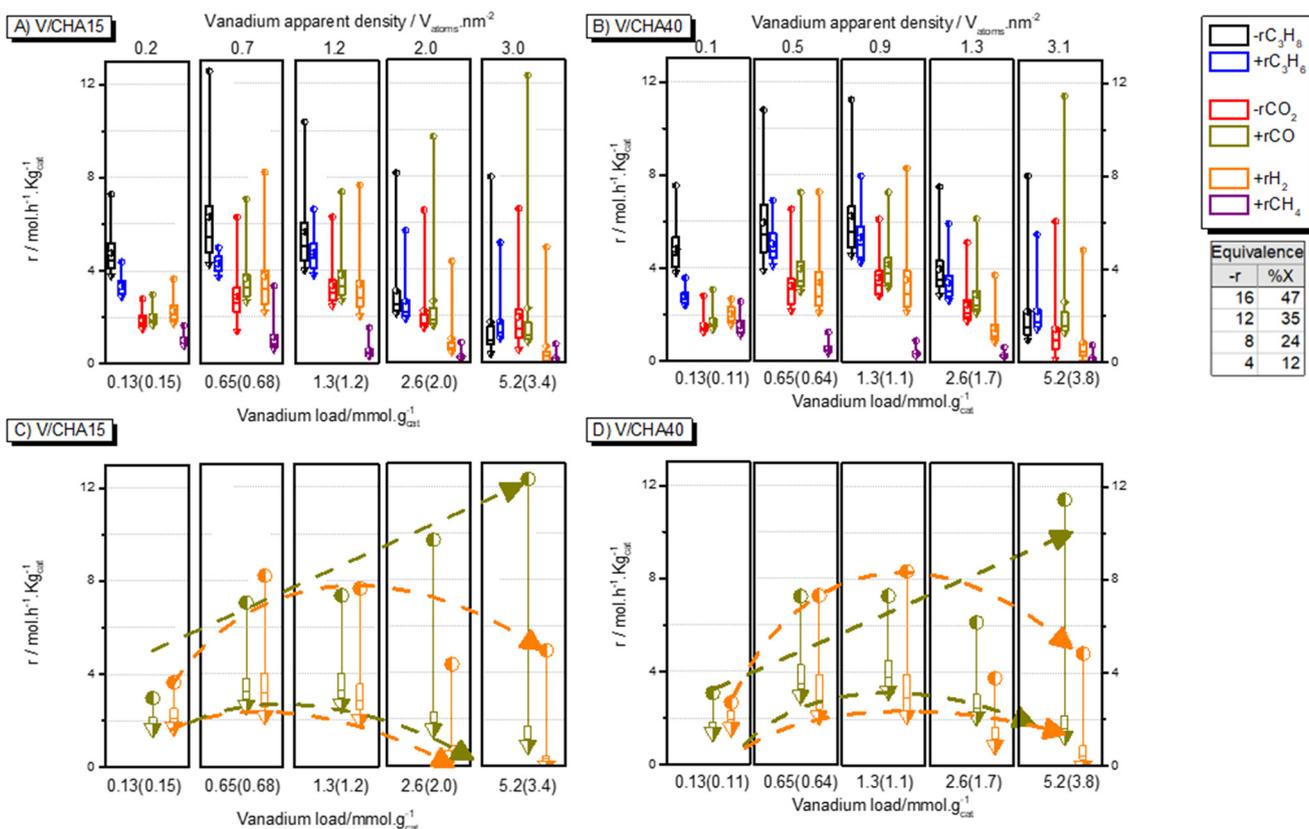
Fig. 4 Impact of vanadium load on the catalytic performance across two CHA supports. (A and B): Catalytic performance study based on reactants consumption and production molar rates. Dual x-axis. Bottom x-axis: nominal load (ICP measured load). Top x-axis: vanadium apparent density. Small inset displays the equivalence between reactant rate consumed and approximate conversion. (C and D) Separate plots highlighting the extreme points (initial and final catalytic profiles) catalytic profile for CO and H_2 production. Reaction at 600 °C using gas ratios of $CO_2/C_3H_8/Ar/N_2$ = 2.5/2.5/47.5/47.5 Nml min^{-1}, GHSV 3.0 × 10^4 Nml gas ml$_{cat}$$^{-1}$ h^{-1}, and WHSV 1.5 g$_{C_3H_8}$ g$_{cat}$$^{-1}$ h^{-1}. For further details, refer to SI Fig. S8–S11. The total time on stream (TOS) duration was 200 minutes, with product sampling conducted every 10 minutes.

materials with tiny pores, with possibilties for pore blockage due to oxide formation, because of the limitations imposed by the BET area determination when small pore zeolite are evaluated.[63] Perhaps a better physical description fits with a gradual depletion of accessibility due to metal oxides causing pore occupancy and the formation of more complex vanadium oxide species. These hypotheses prompted a detailed investigation into the vanadium load in CHA15 and CHA40.

Fig. 4 shows the box and whisker analysis for activity in terms of varying loads of both materials (A and B, respectively). The x-axis (bottom) compares the nominal vanadium content stated for each zeolite (with actual values determined from ICP in brackets)- while the top x-axis shows the vanadium apparent density. Discrepancies are notable beyond a load of 1.3 mmol g^{-1} vanadium (*e.g.*, for the intended load of 5.2 mmol g^{-1} on CHA15, we measured 3.4 mmol g^{-1}). This disparity is more likely due to the metal impregnation method, which involves the depolymerization of vanadate and its dispersion within the support, which becomes more difficult with excessive loads. In such cases, the vanadium solution remains outside the zeolite crystals, making it susceptible to experimental losses. The changing

moisture content in the support and precursor may also have a minor contribution explaining the nominal *versus* measured difference.

The C_3H_6 and H_2 rates exhibit a distinctive volcano-shaped curve with V loading in initial activity for both V/CHA15 and V/CHA40, which is also notable for the average and final TOS levels. To provide additional clarity, we have included separate plots showing a zoom in on their box and whisker plots with guide to the eye lines(Fig. 4C and D). A strong increase in the initial rate, particularly on V/CHA15 at highest loads was observed for CO, *e.g.* to around 12.3 mol h^{-1} kg^{-1}$_{cat}$, which is around double the $+rC_3H_6$ (5.2 mol h^{-1} kg^{-1}$_{cat}$) and $-rCO_2$ (6.6 mol h^{-1} kg^{-1}$_{cat}$) rates (5.2 V/CHA15). This increase is accompanied with 19% of conversion of CO_2 initially for 5.2 V/CHA15. Yet, the average and final rates of CO follow a volcano profile with load (both low and high-pressure data for CHA15 present this effect). In contrast, V/CHA40 mainly maintains the volcano-shaped pattern, even for in its initial CO rates.

A comprehensive analysis of stability and deactivation under varying loads in CHA15 and CHA40 is illustrated in Fig. 5A and B. These plots compare the evolution of pore volume of the fresh catalyst (depicted in purple-white) as
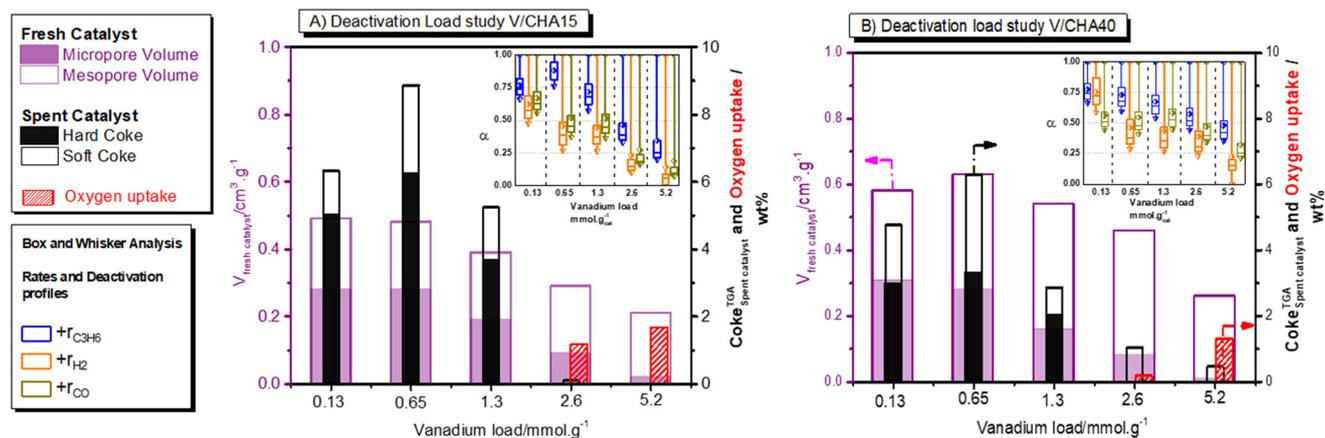
Fig. 5 Impact of vanadium load on the catalytic performance across two CHA supports. (A and B): Assessment of fresh textural properties and comparative deactivation analysis: purple bars and left axis are pore volume by N_2 physisorption. Black and with bars represent coke. Soft coke is the weight loss between 200 C and 600 °C under a nitrogen atmosphere, and hard coke determinate shifting at 600 °C to air. Small inset square: box and whisker plots to illustrate deactivation profiles evaluating the residual activity α (where 1 is the initial activity and 0 correlates with total deactivation). Reaction at 600 °C using gas ratios of $CO_2/C_3H_8/Ar/N_2$ = 2.5/2.5/47.5/47.5 Nml min^{-1}, GHSV 3.0 × 10^4 Nml gas mlcat^{-1} h^{-1}, and WHSV 1.5 g$_{C_3H_8}$ g$_{cat}^{-1}$ h^{-1}. For further details, refer to Fig. S15 and S22.

V-loading increases, with the coke accumulated in spent materials after the final OPDH stage (for different loadings), shown in black-white. Coke was determined and classified as both hard and soft coke. However, our determination of hard coke (>600 °C under air atmosphere) was influenced by a bias: next to mass loss due to the burning of carbon species, we noticed increasing mass resulting from oxygen incorporation during VO$_x$ regeneration (VO$_x$ to V$_2$O$_5$). This phenomenon was not detected in samples with low vanadium loads. However, CHA with loads of 2.6 and 5.2 exhibit significant mass increments (see Fig. 5A and B, red bar), likely still hard coke was produced in the reaction, but less than the increase in mass. We attribute this effect to oxygen uptake, which reached 1.2% and 1.7% values for 2.6 V/CHA15 and 5.2 V/CHA15 and 0.2% and 1.3% for 2.6 V/CHA40 and 5.2 V/CHA40, respectively.

The bias introduced by oxygen uptake in coke TGA measurements is seldom discussed in the literature and remains challenging to quantify accurately. In this study, CHN analyses were conducted for a selection of samples to obtain a reference point for comparison (see Table S6). Ideally, the difference between both techniques reflects that CHN measures net carbon, while TGA captures the total burned mass, including carbon and other elements like hydrogen. In other words, % coke (TGA) should be higher than% C (CHN). However, this expected tendency appeared only in samples with metal loadings below 1.3 mmol g^{-1}. For instance, TGA analysis of the 1.3 V/CHA15 sample showed 5.3% coke, notably higher than the 2.9% carbon reported by CHN. In contrast, the 2.6 V/CHA40 sample exhibited only 0.1% coke as determined by TGA, while CHN reported a six times greater carbon content (0.6%). These discrepancies highlight the influence of oxygen uptake on the coke TGA measurements, especially in samples with metal loadings exceeding 1.3 mmol g$_{cat}^{-1}$. Pure V$_2$O$_5$ nanoparticles subjected

to the same catalytic experiment and analyzed by TGA showed a 7% oxygen uptake, corresponding to an O/V molar ratio of approximately 0.4 (see Fig. S4-C). Notably, the molar ratios of oxygen to vanadium in samples with loads of 2.6 and 5.2 V mmol g^{-1} remain consistent with the V$_2$O$_5$ spent nanoparticles measured. In others words, less than one oxygen per vanadium was determined after reaction in spent materials and V$_2$O$_5$ nanoparticles.

The inserts in Fig. 5A and B present the deactivation profiles based on a relative activity (α), where 1 is the initial activity, and 0 is complete deactivation. The deactivation profiles for the three molecules taken as examples (propylene, H$_2$, and CO) differ, stressing how the catalyst surface dynamic continuously changes by deactivation with molecular-specific effects. Except for the profile for hydrogen of 0.13 V/CHA40, hydrogen shows the highest deactivation (smallest values in each material). Residual activity for both CHAs in the propylene deactivation reveals more stable profiles, especially in 0.65 V/CHA15. The stable activity of propylene is also visible from the short length of the box and whisker plot (even the first quartile) and the proximity between the average (diamond) and the median (horizontal line on the box). Surprisingly, the 0.65 V/CHA15 material reached the highest amount of coke in the series (coherent with the discrepancy between propane consumption and propylene production; see Fig. 4-A).

Notably, at metal loads exceeding 1.3 mmol g^{-1}, CO rates surpass H$_2$ rates. For instance, 0.13 V/CHA15 exhibits higher H$_2$ rates than CO, with an average propylene production of 3.6 mol h^{-1} kg^{-1}, whereas 2.6 V/CHA15 shows a higher CO profile, along an average propylene production of 2.5 mmol h^{-1} kg^{-1}. 0.13 V/CHA15 displays higher tendency to coke with less impact on the activity, with almost 6% coke accumulation leading to a 0.5 decrease in initial activity (α plot inset in Fig. 5A). In contrast, 2.6 V/CHA15, with less than

1 wt% (only) soft coke, experiences nearly total deactivation (around 70–90% of activity loss for all the profiles). The deactivation appears to be predominantly influenced by the first quartile of the experiment (as indicated by a long interquartile range until the box). It is clear from the load and deactivation study that 1.3 V/CHA loadings are kind of optimal, especially when considering average propylene rates, propylene selectivity and CO co-production (that is not from reforming).

Despite the V/CHA15 set having a slightly lower volume micropore in its structure (purple bars in Fig. 5), it accumulated more coke than V/CHA40 at equivalent vanadium nominal loads (Black and white bars Fig. 5). Moreover, the CHA15 catalyst exposes higher deactivation rates than CHA40 materials, as pointed out by the gap between the average (diamonds) and median values (horizontal line) in hydrogen rate associated with coke kinetic (orange plots, inset Fig. 5). Building upon this and recalling the previous observation in cracking (see Fig. 2A and methane in 2B at 1.3 $mmol_v$ g_{cat}^{-1}), the remaining acid sites after metal deposition detracts from propylene selectivity, primarily due to coke formation rather than cracking activity.

Returning to V/CHA accessibility, the balance of metal loading in and on cage-based CHA is crucial for both activity and susceptibility to coke accumulation, which in turn influences the extent of oxidative pathways. The low vanadium load materials show high accessibility and a low degree of vanadium polymerization, resulting in low activity, a high coke accumulation, and more deactivation. With the metal load increments on the series, these materials transition to poorly accessible forms with more complex vanadium oxide structures, which lead to reduced coke formation but significant activity loss. Consequently, an optimal point is observed at a vanadium apparent density of approximately 1.2 V_{atoms} nm^{-2} for CHA15 and 0.9 V_{atoms} nm^{-2} for CHA40. Note that these values, below 2 V_{atoms} nm^{-2} for other supports, reflect a combination of accessibility, vanadium polymerization degree, and complexing, which

must be incorporated into future theoretical models for the reaction. In the context of OPDH, identifying an optimal vanadium load is complex and should be approached cautiously. A vanadium load range between 0.6 to 2.6 appears to be a promising V load region for fine-tuning the catalyst and process design, where the trade-off between oxidative pathways, activity, and coke accumulation needs to be carefully balanced. So far, only 200 minutes TOS experiments were shown. The following section discusses the cyclability of the catalysts over multiple regeneration cycles and extended operation times (Fig. 6).

3.6. Stability and Cyclability test

Fig. 7 and S14 demonstrates that 1.3 V/CHA40 and 1.3 V/CHA70 exhibit superior recyclability and stability compared to 1.3 V/CHA15 and 1.3 V/Al$_2$O$_3$ under reaction conditions simulating industrial conditions (47 kPa partial pressure of propane and CO$_2$, WHSV 1.5 h^{-1}). The experiments involved 10 cycles, each lasting 100 minutes (1.7 hours and quartile size = 25 min), followed by a final stage consisting of a long time-on-stream (1500 minutes = 25 hours and quartile size = 375 min) stability test. An oxidative regeneration step under air was applied between each cycle. See Fig. 6 for all the materials at load 1.3 mmol g^{-1}. 2.6 V/CHA15 failed the test, experiencing total deactivation in the early stages (see Fig. S14). The stability and cyclability test aimed to assess catalyst performance through two stages: short cycles with intermediary regenerations to evaluate activity loss due to irreversible deactivation and a final 25-hour reaction to estimate steady-state yield. While shorter than certain industrial operation requirements (although catofin Cr-systems are regenerated very frequently[1]), this approach provides a comparative metric at the lab scale.

Using the box and whisker analysis of propylene rates, we determined irreversible deactivation based on the average rate of propylene per cycle, indicated by a red line as a guide to eye-tracking the diamonds on the figures. The average rate
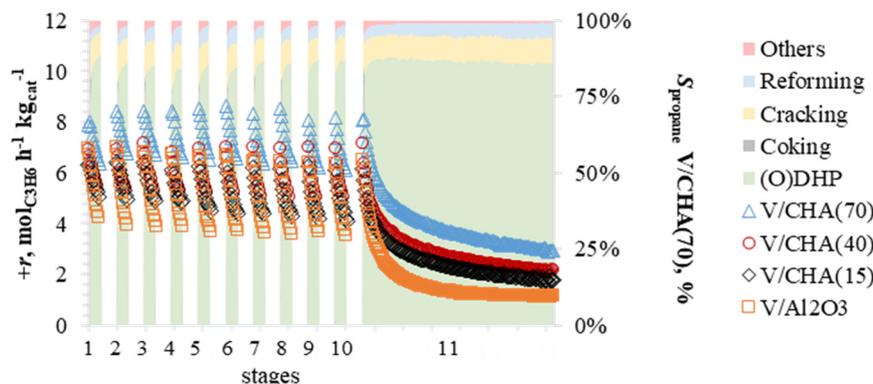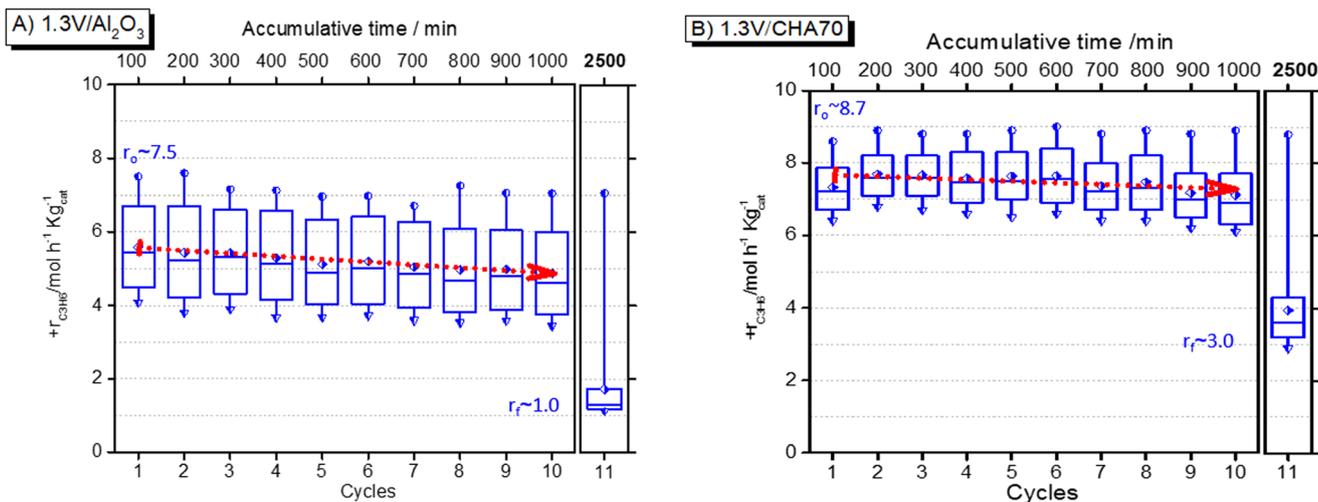

Fig. 6 Recyclability and 24 h stability test: rate of propylene production for 1.3 V/Al$_2$O$_3$, 1.3 V/CHA15, 1.3 V/CHA40 and 1.3 V/CHA70. The selectivity in the background of stages 1 to 11 is plotted for 1.3 V/CHA70. Time per cycle = 100 min. Last stage (cycle 11) = 1500 min. Reaction conditions at 600 °C under 0.9 barg pressure. 200.0(2) mg catalyst of catalyst was used with gas ratios of CO$_2$/C$_3$H$_8$/N$_2$ = 2.5/2.5/5 Nml min^{-1}, GHSV 3.0 × 10^3 Nml$_{gas}$ ml$_{cat}^{-1}$ h^{-1} and WHSV 1.5 g$_{C_3H_8}$ g$_{cat}^{-1}$ h^{-1}. Downstream sampling conducted every 10 minutes.

5308 | *Catal. Sci. Technol.*, 2025, **15**, 5295–5317

This journal is © The Royal Society of Chemistry 2025

Fig. 7 Recyclability and 24 h stability test: box and whisker analysis for propylene production, 10 cycles of 100 min (quartile size = 25 min) and stage 11 of 1500 min (quartile size = 375 min) on A) 1.3 V/Al$_2$O$_3$ and B) 1.3 V/CHA70. Regeneration step with air 10 Nml min^{-1}. Reaction conditions at 600 °C under 0.9 barg pressure. Of catalyst was used with gas ratios of CO$_2$/C$_3$H$_8$/N$_2$ = 2.5/2.5/5 Nml min^{-1}, GHSV 3.0 × 10^3 Nml$_{gas}$ ml$_{cat}$$^{-1}$ h^{-1} and WHSV 1.5 g$_{C_3H_8}$ g$_{cat}$$^{-1}$ h^{-1}. A red dashed arrow is drawn to illustrate the average deactivation trend over the cycles (irreversible deactivation). Note that the last cycle is not comparable due to its extended duration. r_0 = Propylene production at the beginning of the experiment; r_f: propylene production at the end of cycle 11 (end of the experiment).

appears to be the best indicator, as the initial activity involves more experimental variability, and values closer to the steady state (plateau activity after a long time, *e.g.* see stage 11) exhibit less substantial differences.

In this context, 1.3 V/Al$_2$O$_3$ and 1.3 V/CHA15 show a 1.3% to 1.6% decrease in propylene production per regeneration cycle. Meanwhile, 1.3 V/CHA40 and 1.3 V/CHA70 showed a discrete deactivation of around 0.6% per regeneration cycle. In the final stage, cycle 11, 1.3 V/Al$_2$O$_3$ was the only material with an evident profile that reached a quasi-steady state. This conclusion is drawn from the remarkable clustering of the three last quartiles at the end of the experiment, with propylene production close to 1.0 mol h^{-1} kg^{-1}. For the same cycle, all the CHA structures exhibited a slow deactivation continuing until the end of the experiment (indicated by the small distance between the arrowhead and the box on the profile in Fig. 7). However, the best zeolite material, 1.3 V/CHA70, still yielded propylene at a rate exceeding 3.0 mol h^{-1} kg^{-1}, three times higher than that of the 1.3 V/Al$_2$O$_3$ benchmark.

The deactivation mechanism of catalysts following cyclability and stability studies is complex and difficult to pinpoint definitively. However, post-experimental characterization provides valuable insights into the processes contributing to performance decline. A significant observation is the decrease in the XRD signal intensity for the spent samples (see Fig. S24), accompanied by a substantial loss in apparent surface area compared to the fresh materials (see Table S7). This suggests that the catalyst support undergoes structural deterioration during repeated use. Regenerated spent 1.3 V/CHA15 exhibits a surface area reduction of approximately 58%, which aligns with its pronounced deactivation profile. Using the spent 1.3 V/

CHA40 sample as an illustrative case, temperature-programmed reduction (TPR) data shed light on potential metal agglomeration. The hydrogen uptake decreased from 867 μmol g^{-1} in the fresh catalyst to 841 μmol g^{-1} in the regenerated spent material, corresponding to a minor reduction of less than 3%. While this small decrease might suggest limited vanadium aggregation, a more significant indicator is the shift in peak reduction temperatures by +40–50 °C in the spent catalyst. Additionally, obstruction of active sites by debris (from the structural detriment) contribute to the observed changes. This debris might either hinder reduction processes or block access to critical catalytic sites, rendering them less active. Such deterioration could result from structural collapse, pore blockage, or a combination of both, compromising the accessibility of active sites and reducing overall catalytic efficiency.

Thus far, it has been observed that the small crystallite size of the support, high Si/Al ratio, and loading range of 0.65 to 1.3 mmol g^{-1} contribute to enhanced catalytic performance in OPDH. 1.3 V/CHA70, with a zeolite particle size below 0.2 μm, exhibited the best catalytic performance with 33.9% conversion for propane and a simultaneous co-conversion of CO$_2$ of 21.3% with a propylene initial rate of 8.4 mol h^{-1} kg$_{cat}$$^{-1}$ (∼ 0.38 kg$_{C_3H_6}$ h^{-1} kg$_{cat}$$^{-1}$). Moreover, the material demonstrates excellent cyclability and the highest stability compared to the other samples, showing a decrease of only 0.6% of its propylene production rate per regeneration cycle, ensuring good activity even after 10 regenerations and 25 hours of reaction in near-industrial conditions. As a final piece of the study, the following section comprises additional catalytic experiments to gain further insights into this material.
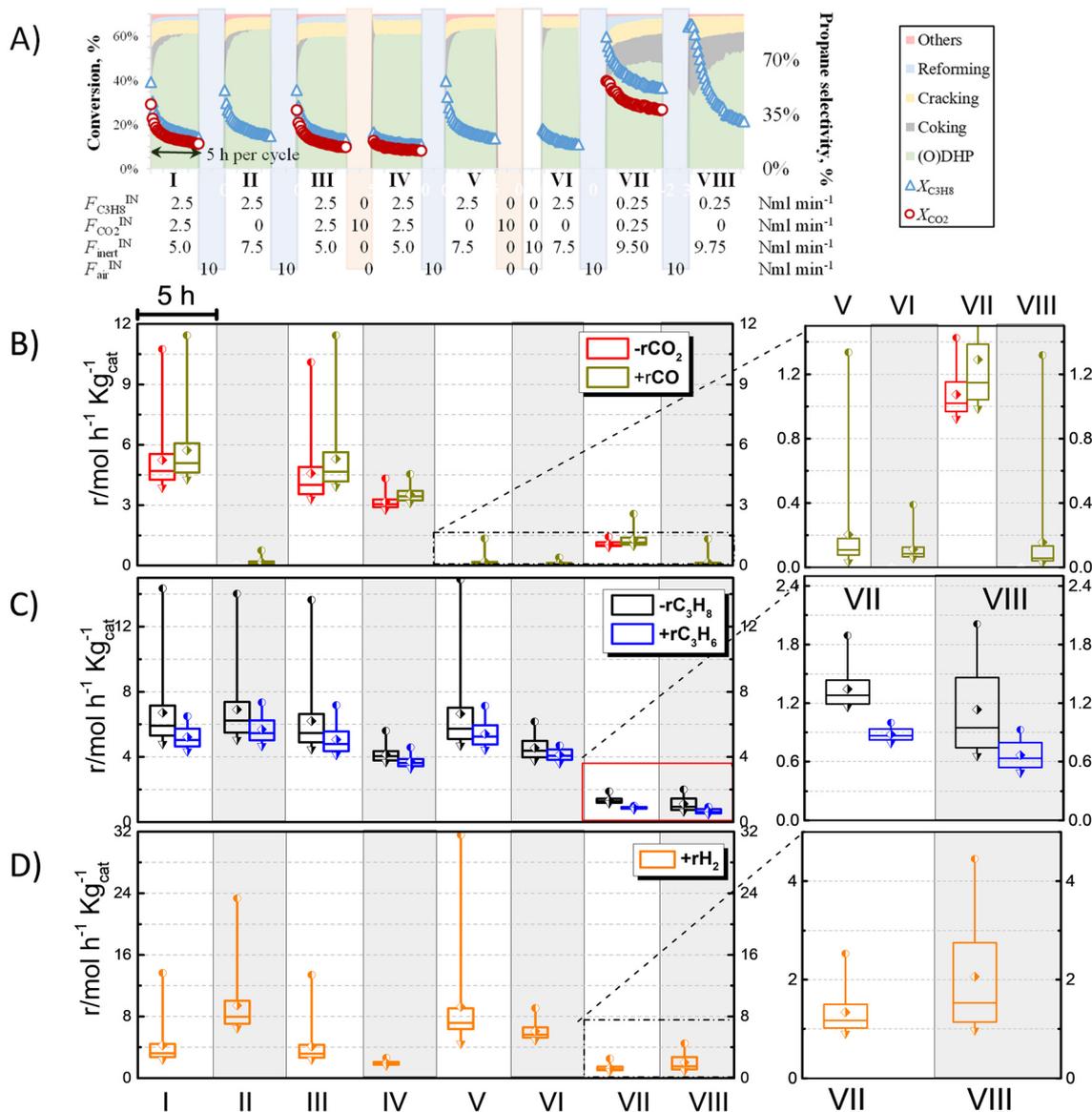
This journal is © The Royal Society of Chemistry 2025

Catal. Sci. Technol., 2025, **15**, 5295–5317 | **5309**

Fig. 8 Variable feed composition applied to 1.3 V/CHA70. A) Propane and CO_2 conversion (left axis) and selectivity (right axis) over 8 cycles (indicated in Roman numerals I-VIII), with a table below detailing the feed composition during each cycle (5 h) and regeneration with F^{IN} representing volumetric flows in Nml min^{-1}. B) Box-and-whisker analysis of propane consumption and propylene production. C) 5 Hour box-and-whisker analysis of CO_2 consumption and CO production. (*i.e. via* ODHP and dry reforming). D) Box-and-whisker analysis of hydrogen production (related to the PDH pathway and deep dehydrogenation). Box and whisker plots excluded the regeneration stages and selected zoom-ins are provided on the right. We loaded 200 mg of V/CHA(70), at a constant T = 600 °C, P = 1 barg. Downstream sampling conducted every 10 minutes.

3.7. Vanadium leaching treatment and catalytic effect of variable feed composition of the 1.3 V/CHA70 catalyst

Alternate PDH/OPDH cycles and a combination of various regeneration conditions were employed to better understand the working active mechanism. Fig. 8A illustrates the conversion and selectivity under all conditions for 1.3 V/CHA70. The whisker and box analysis of the same data is seen in Fig. 8B–D, excluding the regeneration stages. The box and whisker description is as follows: the top plot represents the consumption of CO_2 and the production of CO (OPDH and dry reforming). The quantities of propane converted to propylene

are shown in the middle plot (showing high selectivity if they match). The bottom plot represents H_2 production (associated with the PDH pathway (eqn (1) and 2.1) and deep dehydrogenation). Furthermore, an enlargement of stages V, VI, VII, and VIII is included for more detail. The critical aspects of Fig. 8 can be listed as follows:

When no CO_2 conversion (red profile Fig. 8A) or CO_2 rate (red box and whisker, Fig. 8B) is seen, we are looking at a pure PDH experiment (cycles II, V, VI, and VIII) as evident from the flow inputs (bottom Fig. 8A). Cycle III is a repetition of I in OPDH, and V is a repetition of II in PDH, and the very similar values for the rates in these repetitions confirm the

5310 | *Catal. Sci. Technol.*, 2025, **15**, 5295–5317

This journal is © The Royal Society of Chemistry 2025

cyclability of 1.3 V/CHA70 and show that the effects of long-term deactivation (see discussion Fig. 7) can be neglected in the following discussion. The only outlier in this is the long first quartile whisker for H_2 in PDH (V vs. II). The asymmetric propane consumption with a long first interquartile and lower and more symmetric propylene production indeed suggests a fast coke formation in the initial TOS. This is evident in the case of TOS = 0 and TOS = 75 minutes (start of the box). There is a significant activity loss for propane consumption, from an initial activity around ~14 to a final activity at ~7.2 mol h^{-1} kg^{-1} for both OPDH-I and III and PDH-II and V).

A quite significant CO rate in PDH conditions was observed during cycles V and VIII, with an initial TOS of 1.3 mol h^{-1} kg^{-1} respectively, without complete propylene production deactivation (see arrows in the zoomed regions). The sole source of oxygen originates from the catalyst's transition from VO_x to VO_{x-1}. By performing a molar estimation of the oxygen balance over 5 hours of TOS and considering the current V load (measured by ICP, see Table 2), we determined a molar ratio of $O_{CO-downstream}/V$ of approximately 0.8 per stage. The CO production reflects the kinetics of vanadium species reduction. Notably, cycles V and VIII exhibit the same profile, suggesting that the partial pressure of propane as a reducing agent does not influence this outcome. The discrepancy between CO production and CO_2 consumption under OPDH conditions is explained by the reverse water–gas shift (rWGS) reaction and dry reforming. However, given the changes in the population of V^{+5} during the reaction (e.g. XPS of 1.3 V/CHA70 fresh and spent reported in Table S5) and the CO production under PDH conditions, other side reaction as partial oxidation of hydrocarbons should not be ruled out. Catalyst and process design still face challenges in delaying net vanadium reduction and maintaining V at higher valence states throughout the catalytic cycles, which favors oxidative propylene routes.

The magnification also shows stages VII and VIII, i.e. OPDH and PDH, respectively, where a 10-fold decrease in partial pressure versus those of I and II with same residence time due to more inert atmosphere was applied. Fig. 8A reveals a high conversion due to the lower partial pressure of the reactant and a higher thermodynamic equilibrium (42% for stages I, and III versus 70% for stage VII as the maximum conversion at equilibrium under OPDH reaction conditions for propane and CO_2; and 52% in stages II, and V versus 92% in stage VIII for propane conversion at equilibrium in pure PDH). Despite high conversions in VII and VIII, the selectivity for propylene falls within a range of 60–75% for both stages (= green colored background in Fig. 8A), indicating significant cracking and coking. This suggests that under the reaction conditions, kinetics may be limiting. In other words, while the increase in conversion suggests a sufficient time for reactions to occur, the decrease in selectivity implies that the reaction is not primarily controlled by the diffusion of reactants to or products from the catalyst but instead by the inherent reaction mechanisms themselves. The decrease in selectivity could also indicate potential occurrence of secondary reactions on (adsorbed) products and the formation of undesired products.

A citric acid leaching experiment was designed to target removal of external vanadium species and those accessible to complexes formed with citric acid. The catalyst 1.3 V/CHA70 demonstrated a significant reduction in vanadium content, revealing a notable impact on composition and V-speciation. Bulk vanadium decreased from 1.19 to 0.68 mmol g^{-1}, equivalent to a 42% metal reduction. Fig. 9A display the H_2-TPR profiles of fresh and leached materials which
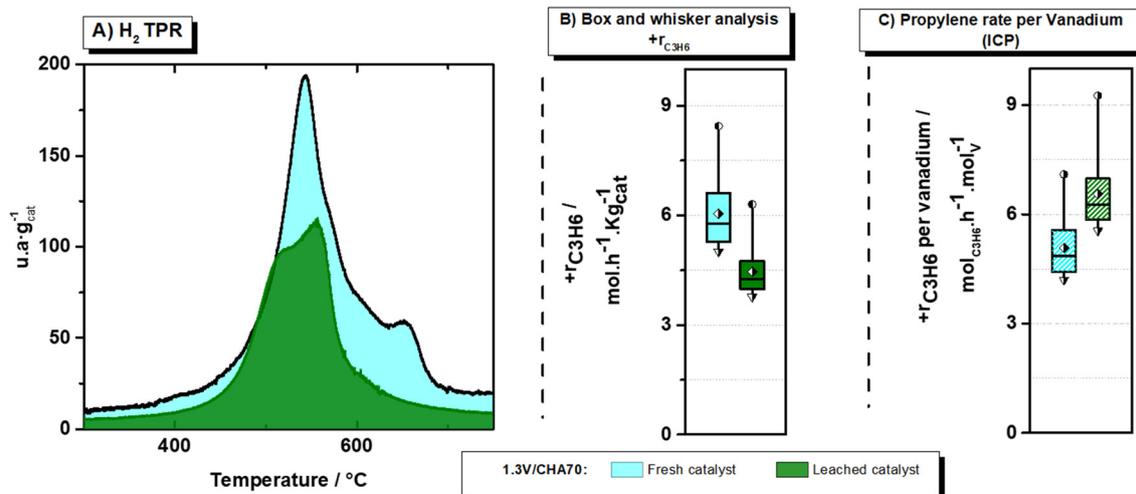

Fig. 9 Vanadium leaching treatment over 1.3 V/CHA70. A) H_2-TPR profile before (fresh) and after leaching; B) box-and-whisker analysis for both leached and fresh catalysts C) box-and-whisker analysis for both leached and fresh catalysts, showing normalized propylene production per mole of vanadium. Reaction at 600 °C for 200.0(2) mg catalyst using gas ratios of $CO_2/C_3H_8/Ar/N_2$ = 2.5/2.5/47.5/47.5 Nml min^{-1}, and WHSV 1.5 $g_{C_3H_8}$ g_{cat}^{-1} h^{-1}. The total time on stream (TOS) duration was 200 minutes, with product sampling conducted every 10 minutes.

This journal is © The Royal Society of Chemistry 2025

Catal. Sci. Technol., 2025, **15**, 5295–5317 | **5311**

corroborates the metal reduction, showing a decrease in hydrogen uptake from 805 to 480 μmol g^{-1}, representing a similar 40% reduction. Interestingly, physisorption analysis of the impregnated and leached samples revealed no significant changes in surface area or pore structure (Fig. S16c). Our observation suggests the citric acid treatment selectively removed vanadium species without extensively altering the overall structural integrity of the CHA support.

Catalytic activity measurements post-leaching showed a systematic reduction of approximately 25% across the catalytic profile, as seen in Fig. 9B. The average catalytic performance, summarized in Fig. 9B, further highlights this reduction shifting from 6 to 4.5 mmol kg$_{cat}$$^{-1}$ h^{-1} (diamond in box and whisker analysis). The lower impact on activity compared to the significant removal of vanadium (42%) suggests that the remaining vanadium species, likely confined within the micropores and certainly less prone to leaching by citric acid, play a bigger role in the catalyst's performance than those removed. Fig. 9C illustrated this by comparing the amount of propylene produced per mole of
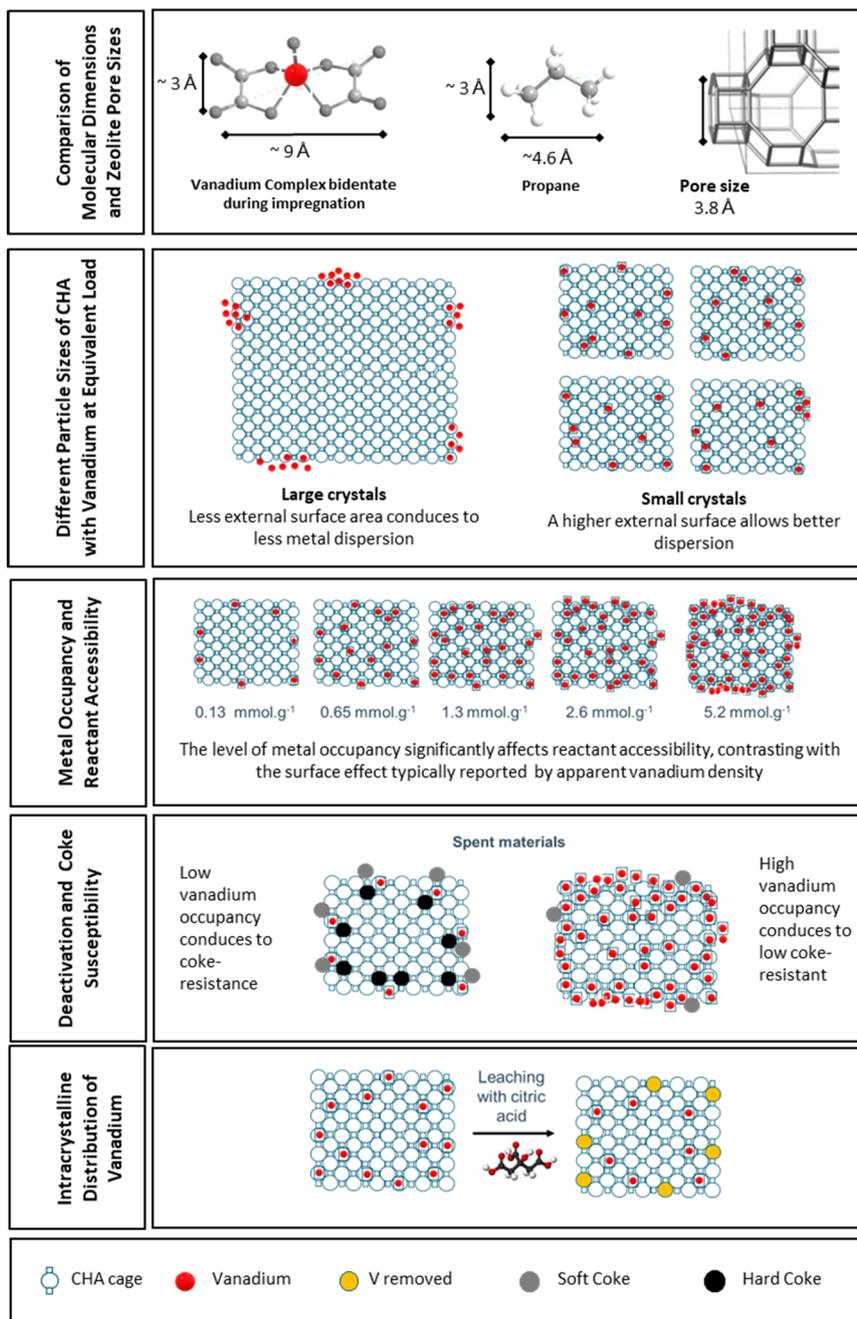
Scheme 1 Key findings and hypothesized conclusions/relationships. This schematic provides a clearer illustration and does not represent the actual number of atoms, the amount of coke formed, or leaching.

vanadium in the catalyst with a superior propylene production for the leached material.

3.8. Key findings and proposed interpretations

Scheme 1 summarizes the key findings and their proposed phenomenological interpretation within the context of the study, highlighting the relationships between the experimental results and the corresponding interpretations.

A simplified static comparison of the molecular dimensions of the vanadium complex (formed during Incipient wetness impregnation), propane, and the pore size of the zeolite (top of Scheme 1) illustrates that the vanadium complex is likely to experience significant diffusion limitations, even greater than those for the reactants. So, crystals with a larger external surface area (*i.e.*, smaller particle size) promote better metal dispersion. This is visually represented as an equivalent vanadium loading per mass, depicted with the same number of red points (vanadium species) distributed across two hypothetical scenarios: first, a large particle and second, four smaller particles, equivalent to the bigger one in mass. Consistent with this, catalysts with chabazite crystal sizes exceeding 1 μm exhibited lower activity and faster deactivation, whereas CHA70, with the smallest crystal size, demonstrated superior catalytic performance. Moreover, it is well established that electrostatic interactions can influence metal dispersion. In this study, NH₃-TPD analysis of 1.3 V/CHA15 (both large and small particle sizes) suggests that metal incorporation does not preferentially target or block acidic sites at least in the loading in question. This behavior could be attributed to the repulsion between the negatively charged zeolite framework and the anionic vanadium complex (*e.g.*, $VO_2(C_2O_4)^-$ in aqueous solution).[69] However, decisive conclusions require deeper studies *in situ* during impregnation.

Increasing metal loading has a dual and contrasting impact on catalytic activity. On one hand, higher metal loading enhances the occupancy of catalyst pores, thereby increasing the number of active sites available for catalysis. On the other hand, each cage occupied by a metal species (or group of them) reduces the accessibility of reactants to the active sites by obstructing the pore structure.

The interplay between these two opposing effects—greater active site density *versus* reduced accessibility—leads to a volcano-shaped relationship when plotting catalytic activity against metal loading. Scheme 1 depicts metal occupancy and accessibility for a small particle CHA. The propensity for CO formation increases with vanadium loading; however, the catalytic profile at later stages of the time on stream (TOS) is predominantly governed by surface coverage due to coke formation. We reach this observation based on the oxygen uptake in spent materials being higher with the higher loading and the linear tendency of CO production at initial catalytic datapoints in the load studies.

The accessibility of the catalytic system significantly affects its susceptibility to coke formation. Catalysts with lower pore volume occupancy by metal exhibit greater resistance to coke accumulation. In other words, these catalysts can tolerate higher levels of organic deposition on their internal surfaces before reaching complete blockage of active sites. In contrast, catalysts with reduced accessibility due to metal-occupied pores require much less coke accumulation to become deactivated. As a result, even the formation of "soft coke" can lead to full deactivation, as discussed earlier. Scheme 1 represents these two extreme cases: first, a material with low metal loading, resulting in minimal metal occupancy in the crystal and a high tolerance for coke formation; and second, a material with high vanadium occupancy, where only a small amount of coke is needed to completely block the crystal.

Finally, at the bottom of Scheme 1, the experiment conducted under citric acid leaching is presented. Based on the hindrance effect of a larger complex with citric acid, we assume that the removal of vanadium species occurs primarily on the external layer of micropore (or directly over the External surface). This likely involves small clusters, monomers, or small polymers deposited on this region accessible to the chemical treatment. Building on this assumption, we demonstrated the existence of intracrystalline vanadium species, which may account for a significant portion of propylene production at least for 1.3 V/CHA70. The three-dimensional micropore system imposes constraints that challenge the assumption of a physical monolayer forming on the internal surfaces. Our results instead indicate an uncontrolled or less controlled formation of V-species.

Conclusions

Here we presented a comprehensive investigation into the potential of loading VO_x onto CHA zeolite supports for CO₂-OPDH. We explored the impact of diverse crystal sizes, aluminum content, and vanadium loadings, as well as different operational conditions. Throughout the study, γ-Al₂O₃ was used as a benchmark support. Our primary aim was to illuminate the viability of small-pore CHA zeolites as alternative supports in contrast to traditional supports with larger pores in the range of macro- and mesoporosity prevalent in the on-purpose propylene industry. Zeolite materials with particle size higher than 1 μm show low activity and fast deactivation. The poor metal dispersion due to the vanadium complex's mass diffusion limitation in the preparation was assigned as the most probable cause. Zeolites with primary (crystal) particle sizes below 1 μm were subjected to a more detailed structure–activity correlation study.

Our analysis revealed that higher aluminium content within the CHA set had adverse effects rather than benefits. Elemental mapping shows vanadium aggregates on the external surface for 1.3 V/CHA15. Our examination of the acid sites before and after impregnation showed minimal changes in acid properties (density and strength) from the metal

This journal is © The Royal Society of Chemistry 2025

Catal. Sci. Technol., 2025, **15**, 5295–5317 | **5313**

impregnation step. The remaining acid sites are likely involved in coke formation which prevails over other side reactions such as cracking, as evidenced in the V-loading study where more significant coke deposition was found on CHA15 compared to CHA40. Furthermore, 1.3 V/CHA40 and 1.3 V/CHA70 demonstrated superior cyclability and stability over 1.3 V/CHA15, reinforcing the observation about the detrimental impact of higher aluminium content. Despite these adverse effects, it was noted that vanadium oxide (VO_x) in more aluminous samples exhibited increased susceptibility to oxidative reactions. This was seen from the initial activity rates of carbon monoxide (CO) production rising with V-loading for CHA15 during metal loading studies, as well as from the elevated oxygen uptake in samples 2.6 V/CHA15 and 5.2 V/CHA during air regeneration.

All small pore V/CHA catalysts revealed a high-pressure sensitivity compared to Al_2O_3. The substantial increase in the rates at initial TOS was particularly noteworthy, leading to nearly double the propylene production rate compared to Al_2O_3. After longer TOS, the beneficial pressure effect subsided. This points to the action of at least two classes of active site (complexes) with the more active ones being somehow more pressure sensitive, likely through their kinetic interaction with (higher partial pressures of) propane and CO_2. When these deactivate, the other type of sites (or propylene production regime) takes over (or is visible), with a more pressure insensitive rate. We dare not speculate on the nature of the sites, although one could suggest that the pressure sensitive ones are inside the cages of the CHA-zeolite. These finding encourage the exploration of higher pressures in (O)PDH research, also in the light of industrial relevance and pressurized CO_2-feeds.

1.3 V/CHA70 exhibited the best activity, selectivity, and stability among the tested catalysts. With propane and CO_2 conversions of 33.9% and 21.3%, respectively. It achieved in initial states approximately 8.4 mmol h^{-1} kg^{-1} of propylene production ($\sim$0.38 $kg_{C_3H_6}$ h^{-1} kg_{cat}^{-1}). Furthermore, the material demonstrated high cyclability and stability, maintaining a propylene production rate of 3 mmol h^{-1} kg^{-1} after 11 regenerations and 2500 minutes (approximately 42 hours) of use. We observed a very minor irreversible deactivation of 0.6% throughout regeneration, less than half of that for the Al_2O_3 benchmark. At the same time, the zeolite had an improved selectivity for CO_2 to CO.

Finally, this study showcases an innovative approach rooted in statistical criteria for evaluating catalytic tests using box and whiskers on molar rates. This method was effectively employed to derive essential activity, selectivity, and stability comparisons. In several sections, we thus managed to analyze 10 catalysts, comparing all activity profiles, reactants, and products at the same time, allowing a more comprehensive analysis of the catalyst dynamics. This strategic approach facilitates comprehensive information management and enables an in-depth exploration of catalytic materials.

Conflicts of interest

There are no conflicts to declare.

Data availability

Acknowledgements

References

1　S. Chen, X. Chang, G. Sun, T. Zhang, Y. Xu, Y. Wang, C. Pei and J. Gong, Propane Dehydrogenation: Catalyst Development, New Chemistry, and Emerging Technologies, *Chem. Soc. Rev.*, 2021, **50**(5), 3315–3354, DOI: **10.1039/d0cs00814a**.

2　B. Feng, Y. C. Wei, W. Y. Song and C. M. Xu, A Review on the Structure-Performance Relationship of the Catalysts during Propane Dehydrogenation Reaction, *Pet. Sci.*, 2022, **19**(2), 819–838, DOI: **10.1016/j.petsci.2021.09.015**.

3　Z. Xu, Y. Yue, X. Bao, Z. Xie and H. Zhu, Propane Dehydrogenation over Pt Clusters Localized at the Sn Single-Site in Zeolite Framework, *ACS Catal.*, 2020, **10**(1), 818–828, DOI: **10.1021/acscatal.9b03527**.

4　K.-X. Li, X. Cai, H.-B. Liu, X.-Y. Liu, Y. Shan, X. Feng and D. Chen, Recent Progress on Catalysts for Propane Dehydrogenation in Presence of CO2, *React. Chem. Eng.*, 2024, **9**, 1292–1312, DOI: **10.1039/D4RE00064A**.

5　M. Marsh and J. Wery, On-purpose propylene production, **https://www.digitalrefining.com/article/1002264/on-purpose-propylene-production**.

6   A. Akah, J. Williams and M. Ghrami, An Overview of Light Olefins Production via Steam Enhanced Catalytic Cracking, *Catal. Surv. Asia*, 2019, **23**(4), 265–276, DOI: **10.1007/s10563-019-09280-6**.

7   C. A. Carrero, R. Schloegl, I. E. Wachs and R. Schomaecker, Critical Literature Review of the Kinetics for the Oxidative Dehydrogenation of Propane over Well-Defined Supported Vanadium Oxide Catalysts, *ACS Catal.*, 2014, **4**(10), 3357–3380, DOI: **10.1021/cs5003417**.

8   D. Mukherjee, S.-E. E. Park and B. M. Reddy, CO_2 as a Soft Oxidant for Oxidative Dehydrogenation Reaction: An Eco Benign Process for Industry, *J. CO2 Util.*, 2016, **16**, 301–312, DOI: **10.1016/j.jcou.2016.08.005**.

9   J. Kang, A. D. Czaja and V. V. Guliants, Carbon Dioxide as Feedstock in Selective Oxidation of Propane, *Eur. J. Inorg. Chem.*, 2017, **2017**(40), 4757–4762, DOI: **10.1002/ejic.201701049**.

10 M. G. Rigamonti, M. Shah, T. G. Gambu, M. Saeys and M. Dusselier, Reshaping the Role of CO2 in Propane Dehydrogenation, from Waste Gas to Platform Chemical, *ACS Catal.*, 2022, 9339–9358, DOI: **10.1021/acscatal.2c01374**.

11 P. Kumar and V. C. Srivastava, Elucidation of Catalytic Propane Dehydrogenation Using Theoretical and Experimental Approaches: Advances and Outlook, *Energy Fuels*, 2023, **37**(23), 18369–18394, DOI: **10.1021/acs.energyfuels.3c02887**.

12 S. Rostom and H. De Lasa, High Propylene Selectivity via Propane Oxidative Dehydrogenation Using a Novel Fluidizable Catalyst: Kinetic Modeling, *Ind. Eng. Chem. Res.*, 2018, **57**(31), 10251–10260, DOI: **10.1021/acs.iecr.8b01891**.

13 S. Rostom and H. De Lasa, Propane Oxidative Dehydrogenation on Vanadium-Based Catalysts under Oxygen-Free Atmospheres, *Catalysts*, 2020, **10**(4), 1–24, DOI: **10.3390/catal10040418**.

14 S. Al-Ghamdi, J. Moreira and H. De Lasa, Kinetic Modeling of Propane Oxidative Dehydrogenation over VOx/γ-Al2O3 Catalysts in the Chemical Reactor Engineering Center Riser Reactor Simulator, *Ind. Eng. Chem. Res.*, 2014, **53**(40), 15317–15332, DOI: **10.1021/ie404064j**.

15 J. A. Mendoza, S. Robijns, I. A. Khan, M. G. Rigamonti, M. L. Bols and M. Dusselier, Support Effects in Vanadium Incipient Wetness Impregnation for Oxidative and Non-Oxidative Propane Dehydrogenation Catalysis, *Catal. Today*, 2024, **430**, 114546, DOI: **10.1016/j.cattod.2024.114546**.

16 R. R. Langeslay, D. M. Kaphan, C. L. Marshall, P. C. Stair, A. P. Sattelberger and M. Delferro, Catalytic Applications of Vanadium: A Mechanistic Perspective, *Chem. Rev.*, 2019, **119**(4), 2128–2191, DOI: **10.1021/acs.chemrev.8b00245**.

17 P. Hu, P. Hu, T. D. Vu, M. Li, S. Wang, Y. Ke, X. Zeng, L. Mai and Y. Long, Vanadium Oxide: Phase Diagrams, Structures, Synthesis, and Applications, *Chem. Rev.*, 2023, **123**(8), 4353–4415, DOI: **10.1021/acs.chemrev.2c00546**.

18 A. S. Sandupatla, S. C. Nayak, C. Sivananda and G. Deo, DFT Investigation into the Experimentally Observed Influence of Oxide Support in the ODH of Propane over Supported Vanadia Catalysts, *Catal. Today*, 2019, **325**(May 2018), 18–24, DOI: **10.1016/j.cattod.2018.05.058**.

19 I. Ascoop, V. V. Galvita, K. Alexopoulos, M.-F. Reyniers, P. Van Der Voort, V. Bliznuk and G. B. Marin, The Role of CO2 in the Dehydrogenation of Propane over WOx–VOx/SiO2, *J. Catal.*, 2016, **335**, 1–10, DOI: **10.1016/j.jcat.2015.12.015**.

20 M. O. Guerrero-Pérez, Supported, Bulk and Bulk-Supported Vanadium Oxide Catalysts: A Short Review with an Historical Perspective, *Catal. Today*, 2017, **285**, 226–233, DOI: **10.1016/j.cattod.2017.01.037**.

21 S. Chakraborty, S. C. Nayak and G. Deo, TiO2/SiO2 Supported Vanadia Catalysts for the ODH of Propane, *Catal. Today*, 2015, **254**, 62–71, DOI: **10.1016/j.cattod.2015.01.047**.

22 M. O. Guerrero-Pérez, V-Containing Mixed Oxide Catalysts for Reduction–Oxidation-Based Reactions with Environmental Applications: A Short Review, *Catalysts*, 2018, **8**, 564, DOI: **10.3390/catal8110564**.

23 D. Shee, T. V. M. Rao and G. Deo, Kinetic Parameter Estimation for Supported Vanadium Oxide Catalysts for Propane ODH Reaction: Effect of Loading and Support, *Catal. Today*, 2006, **118**(3–4 SPEC. ISS), 288–297, DOI: **10.1016/j.cattod.2006.07.017**.

24 K. Routray, K. R. S. Reddy and G. Deo, Oxidative Dehydrogenation of Propane on V2O5/Al2O3 and V2O5/TiO2 Catalysts: Understanding the Effect of Support by Parameter Estimation, *Appl. Catal., A*, 2004, **265**(1), 103–113, DOI: **10.1016/j.apcata.2004.01.006**.

25 X. Jiang, L. Sharma, V. Fung, S. J. Park, C. W. Jones, B. G. Sumpter, J. Baltrusaitis and Z. Wu, Oxidative Dehydrogenation of Propane to Propylene with Soft Oxidants via Heterogeneous Catalysis, *ACS Catal.*, 2021, **11**(4), 2182–2234, DOI: **10.1021/acscatal.0c03999**.

26 K. Chen, A. T. Bell and E. Iglesia, Kinetics and Mechanism of Oxidative Dehydrogenation of Propane on Vanadium, Molybdenum, and Tungsten Oxides, *J. Phys. Chem. B*, 2000, **104**(6), 1292–1299, DOI: **10.1021/jp9933875**.

27 Y. Gambo, S. Adamu, A. A. Abdulrasheed, R. A. Lucky, M. S. Ba-Shammakh and M. M. Hossain, Catalyst Design and Tuning for Oxidative Dehydrogenation of Propane – A Review, *Appl. Catal., A*, 2021, **609**(November 2020), 117914, DOI: **10.1016/j.apcata.2020.117914**.

28 C. Xiong, S. Chen, P. Yang, S. Zha, Z. J. Zhao and J. Gong, Structure-Performance Relationships for Propane Dehydrogenation over Aluminum Supported Vanadium Oxide, *ACS Catal.*, 2019, **9**(7), 5816–5827, DOI: **10.1021/acscatal.8b04701**.

29 Z. Y. Wang, Z. H. He, L. Y. Li, S. Y. Yang, M. X. He, Y. C. Sun, K. Wang, J. G. Chen and Z. T. Liu, Research Progress of CO2 Oxidative Dehydrogenation of Propane to Propylene over Cr-Free Metal Catalysts, *Rare Met.*, 2022, **41**, 2129–2152, DOI: **10.1007/s12598-021-01959-y**.

30 X. Rozanska, R. Fortrie and J. Sauer, Size-Dependent Catalytic Activity of Supported Vanadium Oxide Species: Oxidative Dehydrogenation of Propane, *J. Am. Chem. Soc.*, 2014, **136**(21), 7751–7761, DOI: **10.1021/ja503130z**.

31 C. Chen, M. Sun, Z. Hu, Y. Liu, S. Zhang and Z. Y. Yuan, Nature of Active Phase of VOx Catalysts Supported on SiBeta

This journal is © The Royal Society of Chemistry 2025

Catal. Sci. Technol., 2025, **15**, 5295–5317 | **5315**

for Direct Dehydrogenation of Propane to Propylene, *Chin. J. Catal.*, 2020, **41**(2), 276–285, DOI: **10.1016/S1872-2067(19)63444-3**.

32 I. Ascoop, V. V. Galvita, K. Alexopoulos, M. F. Reyniers, P. Van Der Voort, V. Bliznuk and G. B. Marin, The Role of CO2 in the Dehydrogenation of Propane over WOx-VOx/SiO2, *J. Catal.*, 2016, **335**, 1–10, DOI: **10.1016/j.jcat.2015.12.015**.

33 C. A. Carrero, C. J. Keturakis, A. Orrego, R. Schomäcker and I. E. Wachs, Anomalous Reactivity of Supported V2O5 Nanoparticles for Propane Oxidative Dehydrogenation: Influence of the Vanadium Oxide Precursor, *Dalton Trans.*, 2013, **42**(35), 12644–12653, DOI: **10.1039/c3dt50611h**.

34 J. H. Carter, T. Bere, J. R. Pitchers, D. G. Hewes, B. D. Vandegehuchte, C. J. Kiely, S. H. Taylor and G. J. Hutchings, Direct and Oxidative Dehydrogenation of Propane: From Catalyst Design to Industrial Application, *Green Chem.*, 2021, **23**(24), 9747–9799, DOI: **10.1039/d1gc03700e**.

35 L. Zavala-Sanchez, I. Khalil, L. Oliviero, J. F. Paul and F. Maugé, Structure and Quantification of Edge Sites of WS2/Al2O3 Catalysts Coupling IR/CO Spectroscopy and DFT Calculations, *ChemCatChem*, 2020, **12**(7), 2066–2076, DOI: **10.1002/cctc.201902053**.

36 M. V. Martínez-Huerta, X. Gao, H. Tian, I. E. Wachs, J. L. G. Fierro and M. A. Bañares, Oxidative Dehydrogenation of Ethane to Ethylene over Alumina-Supported Vanadium Oxide Catalysts: Relationship between Molecular Structures and Chemical Reactivity, *Catal. Today*, 2006, **118**(3–4 SPEC. ISS), 279–287, DOI: **10.1016/j.cattod.2006.07.034**.

37 P. Bai, Z. Ma, T. Li, Y. Tian, Z. Zhang, Z. Zhong, W. Xing, P. Wu, X. Liu and Z. Yan, Relationship between Surface Chemistry and Catalytic Performance of Mesoporous γ-Al2O3 Supported VOX Catalyst in Catalytic Dehydrogenation of Propane, *ACS Appl. Mater. Interfaces*, 2016, **8**(39), 25979–25990, DOI: **10.1021/acsami.6b07779**.

38 G. Liu, Z. J. Zhao, T. Wu, L. Zeng and J. Gong, Nature of the Active Sites of VOx/Al2O3 Catalysts for Propane Dehydrogenation, *ACS Catal.*, 2016, **6**(8), 5207–5214, DOI: **10.1021/acscatal.6b00893**.

39 M. Stöcker, Gas Phase Catalysis by Zeolites, *Microporous Mesoporous Mater.*, 2005, **82**(3), 257–292, DOI: **10.1016/j.micromeso.2005.01.039**.

40 M. Moliner, C. Martínez and A. Corma, Synthesis Strategies for Preparing Useful Small Pore Zeolites and Zeotypes for Gas Separations and Catalysis, *Chem. Mater.*, 2014, **26**(1), 246–258, DOI: **10.1021/cm4015095**.

41 M. Dusselier and M. E. Davis, Small-Pore Zeolites: Synthesis and Catalysis, *Chem. Rev.*, 2018, 5265–5329, DOI: **10.1021/acs.chemrev.7b00738**.

42 A. D. Chowdhury, A. L. Paioni, K. Houben, G. T. Whiting, M. Baldus and B. M. Weckhuysen, Bridging the Gap between the Direct and Hydrocarbon Pool Mechanisms of the Methanol-to-Hydrocarbons Process, *Angew. Chem., Int. Ed.*, 2018, **57**(27), 8095–8099, DOI: **10.1002/anie.201803279**.

43 I. Yarulina, A. D. Chowdhury, F. Meirer, B. M. Weckhuysen and J. Gascon, Recent Trends and Fundamental Insights in the Methanol-to-Hydrocarbons Process, *Nat. Catal.*, 2018, **1**(6), 398–411, DOI: **10.1038/s41929-018-0078-5**.

44 P. Tian, Y. Wei, M. Ye and Z. Liu, Methanol to Olefins (MTO): From Fundamentals to Commercialization, *ACS Catal.*, 2015, **5**(3), 1922–1938, DOI: **10.1021/acscatal.5b00007**.

45 C. Paolucci, A. A. Parekh, I. Khurana, J. R. Di Iorio, H. Li, J. D. A. Caballero, A. J. Shih, T. Anggara, W. N. Delgass, J. T. Miller, F. H. Ribeiro, R. Gounder and W. F. Schneider, Catalysis in a Cage: Condition-Dependent Speciation and Dynamics of Exchanged Cu Cations in SSZ-13 Zeolites, *J. Am. Chem. Soc.*, 2016, **138**, 6028–6048, DOI: **10.1021/jacs.6b02651**.

46 J. H. Kwak, R. G. Tonkyn, D. H. Kim, J. Szanyi and C. H. F. Peden, Excellent Activity and Selectivity of Cu-SSZ-13 in the Selective Catalytic Reduction of NOx with NH3, *J. Catal.*, 2010, **275**(2), 187–190, DOI: **10.1016/J.JCAT.2010.07.031**.

47 R. Gounder and A. Moini, Automotive NO: X Abatement Using Zeolite-Based Technologies, *React. Chem. Eng.*, 2019, **4**(6), 966–968, DOI: **10.1039/c9re90030f**.

48 F. Gao and C. H. F. Peden, Recent Progress in Atomic-Level Understanding of Cu/SSZ-13 Selective Catalytic Reduction Catalysts, *Catalysts*, 2018, **8**(140), 1–23, DOI: **10.3390/catal8040140**.

49 Y. Yuan and R. F. Lobo, Propane Dehydrogenation over Extra-Framework In(i) in Chabazite Zeolites, *Chem. Sci.*, 2022, **13**(10), 2954–2964, DOI: **10.1039/d1sc05866e**.

50 J. Pan, J. Lee, M. Li, B. A. Trump and R. F. Lobo, Comparative Investigation of Ga- and In-CHA in the Non-Oxidative Ethane Dehydrogenation Reaction, *J. Catal.*, 2022, **413**, 812–820, DOI: **10.1016/j.jcat.2022.07.018**.

51 Y. Yuan, J. S. Lee and R. F. Lobo, Ga+-Chabazite Zeolite: A Highly Selective Catalyst for Nonoxidative Propane Dehydrogenation, *J. Am. Chem. Soc.*, 2022, **144**(33), 15079–15092, DOI: **10.1021/jacs.2c03941**.

52 H. Fu, H. Ma, W. Qian, H. Zhang and W. Ying, Copper-Promoted Platinum Supported on HSSZ-13 Zeolite Catalysts for Propane Dehydrogenation to Propylene, *Energy Fuels*, 2024, **38**(9), 8072–8083, DOI: **10.1021/acs.energyfuels.4c00469**.

53 Z. Sun, Z. Zhu, H. Zhang, C. Chu, D. Han, J. Zhang, F. Wang, L. Bing and G. Wang, Nano-Hierarchical SSZ-13-Supported Low-Polymerized VOX as Highly Efficient Catalysts for Propane Dehydrogenation, *Ind. Eng. Chem. Res.*, 2024, **61**, 7614–7623, DOI: **10.1021/acs.iecr.4c00356**.

54 Y. Jiang, W. Zhou, N. He, S. Yang, S. Chen and J. Liu, Preparation of Shaped Binder-Free SSZ-13 Zeolite and Its Aplication in CO2 Adsorption and Catalysis, *ChemCatChem*, 2022, **7**(2), 2013–2015, DOI: **10.1002/cctc.202200795**.

55 D. Fu, Y. Park and M. E. Davis, Zinc Containing Small-Pore Zeolites for Capture of Low Concentration Carbon Dioxide, *Angew. Chem., Int. Ed.*, 2022, **61**(5), 1–6, DOI: **10.1002/anie.202112916**.

56 J. Liu, N. He, Z. Zhang, J. Yang, X. Jiang, Z. Zhang, J. Su, M. Shu, R. Si, G. Xiong, H. B. Xie and G. Vilé, Highly-Dispersed Zinc Species on Zeolites for the Continuous and Selective Dehydrogenation of Ethane with CO2as a Soft Oxidant, *ACS Catal.*, 2021, **11**(5), 2819–2830, DOI: **10.1021/acscatal.1c00126**.

5316 | *Catal. Sci. Technol.*, 2025, **15**, 5295–5317

This journal is © The Royal Society of Chemistry 2025

57 J. Devos, S. Robijns, C. Van Goethem, I. Khalil and M. Dusselier, Interzeolite Conversion and the Role of Aluminum: Toward Generic Principles of Acid Site Genesis and Distributions in ZSM-5 and SSZ-13, *Chem. Mater.*, 2021, **33**(7), 2516–2531, DOI: **10.1021/acs. chemmater.0c04832**.

58 J. Devos, M. L. Bols, D. Plessers, C. Van Goethem, J. W. Seo, S. J. Hwang, B. F. Sels and M. Dusselier, Synthesis-Structure-Activity Relations in Fe-CHA for C–H Activation: Control of Al Distribution by Interzeolite Conversion, *Chem. Mater.*, 2020, **32**(1), 273–285, DOI: **10.1021/acs.chemmater.9b03738**.

59 J. Devos, M. A. Shah and M. Dusselier, On the Key Role of Aluminium and Other Heteroatoms during Interzeolite Conversion Synthesis, *RSC Adv.*, 2021, 26188–26210, DOI: **10.1039/d1ra02887a**.

60 J. R. Di Iorio and R. Gounder, Controlling the Isolation and Pairing of Aluminum in Chabazite Zeolites Using Mixtures of Organic and Inorganic Structure-Directing Agents, *Chem. Mater.*, 2016, **28**(7), 2236–2247, DOI: **10.1021/acs. chemmater.6b00181**.

61 M.-J. Díaz-Cabañas and P. A. Barrett, Synthesis and Structure of Pure SiO2 Chabazite: The SiO2 Polymorph with the Lowest Framework Density, *Chem. Commun.*, 1998, 1881–1882, DOI: **10.1039/A804800B**.

62 N. Asim, S. Radiman, M. A. Yarmo and M. S. Banaye Golriz, Vanadium Pentoxide: Synthesis and Characterization of Nanorod and Nanoparticle V2O5 Using CTAB Micelle Solution, *Microporous Mesoporous Mater.*, 2009, **120**(3), 397–401, DOI: **10.1016/j.micromeso.2008.12.013**.

63 M. Thommes, K. Kaneko, A. V. Neimark, J. P. Olivier, F. Rodriguez-Reinoso, J. Rouquerol and K. S. W. Sing, Physisorption of Gases, with Special Reference to the Evaluation of Surface Area and Pore Size Distribution (IUPAC Technical Report), *Pure Appl. Chem.*, 2015, **87**(9–10), 1051–1069, DOI: **10.1515/pac-2014-1117**.

64 E. V. Kondratenko, M. Cherian and M. Baerns, Oxidative Dehydrogenation of Propane over Differently Structured Vanadia-Based Catalysts in the Presence of O2 and N2O, *Catal. Today*, 2006, **112**(1–4), 60–63, DOI: **10.1016/j. cattod.2005.11.028**.

65 J. T. Grant, C. A. Carrero, A. M. Love, R. Verel and I. Hermans, Enhanced Two-Dimensional Dispersion of Group v Metal Oxides on Silica, *ACS Catal.*, 2015, **5**(10), 5787–5793, DOI: **10.1021/acscatal.5b01679**.

66 M. Jacquemin, M. J. Genet, E. M. Gaigneaux and D. P. Debecker, Calibration of the X-Ray Photoelectron Spectroscopy Binding Energy Scale for the Characterization of Heterogeneous Catalysts: Is Everything Really under Control?, *ChemPhysChem*, 2013, **14**(15), 3618–3626, DOI: **10.1002/cphc.201300411**.

67 Z. Gromotka, G. Yablonsky, N. Ostrovskii and D. Constales, Three-Factor Kinetic Equation of Catalyst Deactivation, *Entropy*, 2021, **23**(7), 1–22, DOI: **10.3390/e23070818**.

68 M. Guisnet, L. Costa and F. R. Ribeiro, Prevention of Zeolite Deactivation by Coking, *J. Mol. Catal. A: Chem.*, 2009, **305**(1–2), 69–83, DOI: **10.1016/j.molcata.2008.11.012**.

69 V. I. E. Bruyère, L. A. Garcia Rodenas, P. J. Morando and M. A. Blesa, Reduction of Vanadium(V) by Oxalic Acid in Aqueous Acid Solutions, *J. Chem. Soc., Dalton Trans.*, 2001, **24**, 3593–3597, DOI: **10.1039/b103320b**.

70 J. M. Kanervo, M. E. Harlin, A. O. I. Krause and M. A. Bañares, Characterisation of Alumina-Supported Vanadium Oxide Catalysts by Kinetic Analysis of H2-TPR Data, *Catal. Today*, 2003, **78**, 171–180, DOI: **10.1016/S0920-5861(02)00326-7**.

71 C. Hess, G. Tzolova-Müller and R. Herbert, The Influence of Water on the Dispersion of Vanadia Supported on Silica SBA-15: A Combined XPS and Raman Study, *J. Phys. Chem. C*, 2007, **111**(26), 9471–9479, DOI: **10.1021/jp0713920**.

72 G. Silversmit, D. Depla, H. Poelman, G. B. Marin and R. De Gryse, Determination of the V2p XPS Binding Energies for Different Vanadium Oxidation States (V5+ to V0+), *J. Electron Spectrosc. Relat. Phenom.*, 2004, **135**(2–3), 167–175, DOI: **10.1016/j.elspec.2004.03.004**.

73 M. C. Biesinger, L. W. M. Lau, A. R. Gerson and R. S. C. Smart, Resolving Surface Chemical States in XPS Analysis of First Row Transition Metals, Oxides and Hydroxides: Sc, Ti, V, Cu and Zn, *Appl. Surf. Sci.*, 2010, **257**(3), 887–898, DOI: **10.1016/j.apsusc.2010.07.086**.

74 R. Chlosta, G. Tzolova-Müller, R. Schlögl and C. Hess, Nature of Dispersed Vanadium Oxide: Influence of the Silica Support Structure and Synthesis Methods, *Catal. Sci. Technol.*, 2011, **1**(7), 1175–1181, DOI: **10.1039/c1cy00062d**.

75 Y. Li, X. Yu, Q. Zhang, V. A. Kondratenko, Y. Wang, G. Cui, M. Zhou, C. Xu, E. V. Kondratenko and G. Jiang, The Nature of VOx Structures in HMS Supported Vanadium Catalysts for Non-Oxidative Propane Dehydrogenation, *J. Catal.*, 2022, **413**, 658–667, DOI: **10.1016/j.jcat.2022.07.017**.

76 J. H. Carter, T. Ye, D. G. Hewes, A. Almoteiry, K. J. Aggett, B. D. Vandegehuchte, C. J. Kiely, S. H. Taylor and G. J. Hutchings, Origin of Carbon Monoxide Formation in the Oxidative Dehydrogenation of Propane Using Carbon Dioxide, *ACS Catal.*, 2024, **14**(15), 11881–11892, DOI: **10.1021/acscatal.4c02628**.

77 M. V. Martínez-Huerta, J. M. Coronado, M. Fernández-García, A. Iglesias-Juez, G. Deo, J. L. G. Fierro and M. A. Bañares, Nature of the Vanadia-Ceria Interface in V5+/CeO2 Catalysts and Its Relevance for the Solid-State Reaction toward CeVO4 and Catalytic Properties, *J. Catal.*, 2004, **225**(1), 240–248, DOI: **10.1016/j.jcat.2004.04.005**.

78 A. Khodakov, J. Yang, S. Su, E. Iglesia and A. T. Bell, Structure and Properties of Vanadium Oxide-Zirconia Catalysts for Propane Oxidative Dehydrogenation, *J. Catal.*, 1998, **177**(2), 343–351, DOI: **10.1006/jcat.1998.2143**.

79 X. Gao, S. R. Bare, B. M. Weckhuysen and I. E. Wachs, In Situ Spectroscopic Investigation of Molecular Structures of Highly Dispersed Vanadiumoxide on Silica under Various Conditions, *J. Phys. Chem. B*, 1998, **102**(52), 10842–10852, DOI: **10.1021/jp9826367**.

80 H. Tian, E. I. Ross and I. E. Wachs, Quantitative Determination of the Speciation of Surface Vanadium Oxides and Their Catalytic Activity, *J. Phys. Chem. B*, 2006, **110**(19), 9593–9600, DOI: **10.1021/jp055767y**.

This journal is © The Royal Society of Chemistry 2025

Catal. Sci. Technol., 2025, **15**, 5295–5317 | **5317**